Model Catalysis – Single Crystal Surfaces and Graphene-Supported Metal Nanocluster Arrays Studied by In Situ High Resolution XPS

Modellkatalyse – Untersuchung von Einkristalloberflächen und regelmäßig angeordneten Nanopartikeln auf Graphen mittels hochaufgelöster *in situ* Röntgenphotoelektronenspektroskopie

Der Naturwissenschaftlichen Fakultät

der Friedrich-Alexander-Universität Erlangen-Nürnberg

zur Erlangung des Doktorgrades Dr. rer. nat.

vorgelegt von

KARIN GOTTERBARM

aus München

Als Dissertation genehmigt von der Naturwissenschaftlichen Fakultät
der Friedrich-Alexander-Universität Erlangen-Nürnberg

Tag der mündlichen Prüfung: 20.07.2015

Vorsitzender des Promotionsorgans: Prof. Dr. Johannes Barth

Gutachter: Prof. Dr. Hans-Peter Steinrück
                    Prof. Dr. Andreas Görling

Drum hab ich mich der *Chemie* ergeben:

Dass ich erkenne, was die Welt

im Innersten zusammenhält.

frei nach Faust (J.W. Goethe)

Forschung beginnt immer mit Neugier.

(G. Ertl)

Kurzzusammenfassung

Heterogene Katalysatoren sind von großer wirtschaftlicher und ökologischer Bedeutung. Um die heterogene Katalyse auf atomarer Ebene zu verstehen, ist es erforderlich, Modellsysteme mit definierten Eigenschaften zu untersuchen. Ein wichtiger Aspekt im Hinblick auf katalytische Aktivität ist die Katalysatorvergiftung durch atomaren Schwefel und Schwefeloxide. Zur Untersuchung dieses Phänomens wurde SO_2 auf der Pd(100) Oberfläche durch Erwärmen schrittweise zu atomarem Schwefel reduziert. Im Gegenzug konnten Schwefelverunreinigungen in einer sauerstoffreichen Atmosphäre effektiv durch Oxidation entfernt werden. Der Oxidationsprozess verläuft schrittweise bis hin zu SO_4, welches letztendlich zerfällt und von der Oberfkäche desorbiert. Als ein Schritt in Richtung realer Katalysatorsysteme wurden die Eigenschaften und Reaktivität von Nanopartikeln auf Graphen untersucht. Die Untersuchung verschiedener Wachstumsparameter ergibt, dass eine Probentemperatur von 920 K und ein Druck des Kohlenstoffpräkursors Propen oder Ethen von $2 \cdot 10^8$ mbar ideal sind, um durch chemische Gasphasenabscheidung Graphenschichten mit möglichst geringer Defektdichte auf der Rh(111) Oberfläche zu erzeugen. Nanocluster aus Palladium und Platin werden durch Elektronenstoßverdampfung abgeschieden. Auf Rh(111) bildet Graphen eine Moiré-Struktur, die als Templat für die Nanocluster fungiert. Dadurch sind die Größe und Verteilung der Nanopartikel durch die Dimensionen des Moirégitters von Graphen auf Rh(111) bestimmt. Die Partikel sind bis 550 K stabil, agglomerieren bis 750 K und interkalieren bei höheren Temperaturen zwischen der Graphenschicht und der Rhodiumoberfläche. Die eingehende Analyse der photoelektronenspektroskopischen Spektren der Metall- und Adsorbatorbitale sowie der Vergleich mit Einkristalldaten ermöglichen detaillierte Erkenntnisse über die Adsorptionseigenschaften von CO und SO_2 auf Nanopartikeln auf Graphen. Sowohl Pd- als auch Pt- Partikel sind aus einer Mischung von niedrig indizierten Facetten und Stufen aufgebaut. Wegen der unterschiedlichen Koordination an Stufen unterschiedlicher Geometrie weisen CO und SO_2 gegensätzliche Adsorptionspräferenzen auf den Pt Nanopartikeln aus: während CO bevorzugt auf (111) Stufen adsorbiert, besetzt SO_2 vorrangig (100) Stufen. Beim Erwärmen diffundiert SO_2 auf die Stufen und reagiert bei höheren Temperaturen zu SO_3 und atomarem Schwefel. Weiterhin wird bei der isothermen Oxidation von CO eine Kinetik pseudo-erster Ordnung und eine wesentlich kleinere Aktivierungsenergie als auf Pt(111) gefunden. Die geringe Aktivierungsenergie der CO Oxidation und die große Menge von entstandenem Schwefel bestätigen die außergewöhnliche Reaktivität der Nanopartikel.

Abstract

Model catalysts with defined properties are necessary to understand heterogeneous catalytic processes on the atomic level. One important aspect of catalytic activity, namely poisoning with atomic sulfur and sulfur oxides, was investigated on the Pd(100) surface. On Pd(100), SO_2 is reduced stepwise to atomic sulfur upon heating. However, in an oxygen-rich environment sulfur is removed effectively from the surface by oxidation. The oxidation proceeds stepwise to SO, SO_2, SO_3 and SO_4, which finally decomposes and desorbs from the surface. As a step towards the more complex structure of real catalysts, the properties and reactivity of graphene-supported nanocluster arrays were studied in detail. Due to their narrow size distribution and the chemically innocent substrate, these systems represent intriguing model catalysts. The variation of CVD growth parameters reveals that a sample temperature of 920 K and a carbon precursor pressure of $2 \cdot 10^{-8}$ mbar ideal for the preparation of graphene layers with a low defect density on Rh(111). Pd and Pt nanoclusters are deposited by electron beam evaporation. Due to a template-assisted growth process, the size and distribution of the nanoclusters are governed by the dimensions of the Moiré unit cell of Gr/Rh(111). The clusters are stable until 550 K, agglomerate until 750 K and intercalate between Rh and Gr at higher temperatures. The extensive analysis of core level spectra of the metal substrate and of the adsorbate, and the comparison to single crystal data allow for a detailed insight into the adsorption properties of graphene-supported nanoclusters. Both Pd and Pt clusters consist of a mixture of low-index facets and steps. For the Pt nanoclusters, significant differences to single crystal surfaces are observed due to the electronic influence of the steps. The adsorption energies of CO at different adsorption sites on the cluster facets differ from those on Pt(111). CO and SO_2 exhibit contrary adsorption preferences at the steps of the Pt nanoclusters: While CO preferentially adsorbs at (111) steps, SO_2 occupies (100) steps to a higher extent. Upon heating, SO_2 diffuses to the steps, and disproportionates to SO_3 and atomic sulfur at higher temperatures. The isothermal oxidation of CO on Pt nanoclusters exhibits pseudo-first-order kinetics and a comparably small activation energy. The small activation energy for CO oxidation and high amount of produced sulfur confirm the enhanced reactivity of the nanoclusters.

Contents

1   Model catalysts – from single crystals to nanoclusters

Heterogeneous catalysts play an important role in the production of various chemicals,[1] oil-reforming,[2] and exhaust gas purification in both industrial processes and the automotive catalytic converter.[3-8] Typically, commercial catalysts consist of nanoparticles of a catalytically active metal or metal oxide dispersed on an oxidic support material, e.g. ceria or alumina. The performance and selectivity of a catalyst is determined by a variety of different factors: the nature of the catalytically active metal as well as the support material, the surface area, the size and shape of the metal particles, the nature and number of defects, and support-related effects such as spillover and reverse spillover.[8-14] Additionally, the long-time performance is influenced by poisoning.[15-17] Typical poisons are atomic sulfur and its sulfur oxides, SO_x (x = 1 – 4), that are known to cause severe catalyst poisoning[17-23] and furthermore pose a threat to the environment by causing acid rain[24]. In order to be able to design heterogeneous catalysts with tailored properties in a knowledge-driven approach, it is necessary to understand catalytic processes on the atomic level. Due to the aforementioned complexity of industrial heterogeneous catalysts, this is not easily achieved. Therefore, fundamental research has focused on systems that model certain properties of industrial catalysts while being simple enough to be thoroughly understood. The increasing complexity, from several different model systems to commercial catalysts, is shown in Figure 1.1.

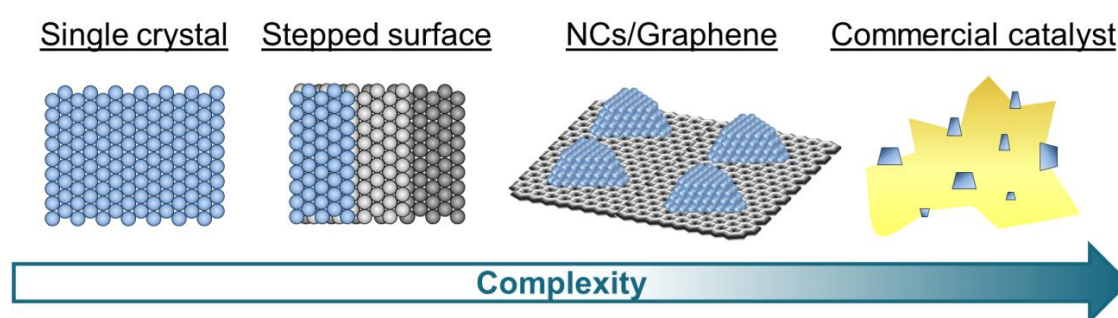*Figure 1.1: Increasing complexity from different model systems to commercial heterogeneous catalysts.*

The simplest model for the adsorption and reaction on the facets of catalyst particles is a low-index single crystal surface. These model systems have been in the focus of surface science in the past 50 years, and have been investigated in detail with great success. In 2007, G. Ertl was even awarded the Nobel Prize in

chemistry for his studies of chemical processes on such solid surfaces.[25] Typically, the single crystals are placed in a very clean ultra-high vacuum (UHV) environment to avoid surface contaminations. A variety of different surface sensitive experimental methods are available: low energy electron diffraction (LEED), thermal desorption spectroscopy (TDS), electron energy loss spectroscopy (EELS), infrared reflection absorption spectroscopy (IRAS), near edge X-ray absorption fine structure (NEXAFS), X-ray and UV photoelectron spectroscopy (XPS and UPS), scanning tunneling microscopy (STM), and atomic force microscopy (AFM), amongst others.[7-8, 26-28] Additional insight is gained from the comparison of experimental results with theoretical predictions from density functional theory (DFT). With the combination of these methods, it has been possible to determine ordered surface structures,[29-32] nature and orientation of surface species,[33-34] specific adsorption sites,[35-37] adsorption energies,[35, 38-39] intermediate reaction species,[33-34, 40-41] and even activation energies of reactions on surfaces.[40, 42-43]

These flat single crystal surfaces are the simplest model for a heterogeneous catalyst, because only the reaction on the facets of the metal clusters is reproduced. However, it has been proposed that especially step sites and highly coordinated kink sites are responsible for the high catalytic activity of small metal clusters.[1, 7-8, 44] This discrepancy has been referred to as the materials gap between catalysis and surface science.[45-47] One way to introduce more complexity into the model systems is the investigation of stepped single crystal surfaces. The presence of steps provides new adsorption sites. In addition, more extensive differences to flat single crystal surfaces have been observed: adsorption energies may differ from those on flat surfaces,[48-49] varying preferred adsorption geometries were found on differently stepped surfaces,[34] higher reactivities of the stepped surfaces are observed,[34, 50-51] and on particular surfaces even the dissociation of adsorbate species, which remain intact on the corresponding flat surfaces, was discovered.[52-53] These differences are attributed to the higher coordinated adsorption sites and the electronic influence of the steps. In this thesis, two different stepped surfaces are discussed in detail: Pt(355) and Pt(322). Both surfaces consist of five atom wide (111) terraces, but contain steps with different orientation. On Pt(355) the steps exhibit a (111) orientation (see example in Figure 1.1), while on Pt(322) the steps are oriented in the (100) direction.

The divergent adsorption properties of flat and stepped single crystal surfaces prove that complex catalytic systems cannot simply be described by a

sum of different adsorption sites, but interactions between all included components have to be considered carefully. Therefore, it is necessary to find suitable model systems that are even closer to real catalysts, while still avoiding undesirable effects that complicate a detailed analysis. To eliminate support-related effects like spillover,[14] a chemically innocent support material is preferable. Furthermore, the catalytically active metal clusters on the support should be monodisperse or exhibit a very narrow size distribution. If this is the case, averaging over various particle sizes does not have to be taken into account. This thesis focuses on a novel class of model systems that employs the template effect of the graphene Moiré structure on a lattice-mismatched substrate. With this fabrication method, regular arrays of metal nanoclusters with a narrow size distribution on a chemically innocent support are produced.

Graphene (Gr) is produced by a chemical vapor deposition (CVD) process on a number of different metal surfaces.[54-56] The metal surface is annealed while a carbon precursor like ethane, ethene, propene or benzene is supplied. If the surface temperature is sufficiently high, the carbon precursor is cracked, hydrogen desorbs from the surface and the remaining carbon fragments form graphene. By choosing a precursor that contains heteroatoms like boron or nitrogen, also differently doped graphene layers can be produced with this method.[57-58] Depending on the used metal, the precursor pressure and surface temperature have to be adjusted to yield a defect-free graphene layer.[54, 59] On metal substrates, which exhibit a lattice mismatch with graphene, such as Pt(111),[59-60] Ir(111),[61-63] Rh(111),[64-65] or Ru(0001),[66-68] a Moiré superstructure with a larger unit cell than that of Gr or Rh is observed. In different regions of the Moiré unit cell, the carbon atoms of the overlaying graphene layer occupy different adsorption sites and therefore exhibit a different interaction with the metal substrate. This difference in interaction strength leads to varying vertical distances of the carbon atoms in the graphene layer over the metal substrate along the unit cell of the Moiré super-structure. The resulting periodic vertical modulation of the graphene layer is used as template for the fabrication of metal nanocluster arrays. N'Diaye et al. first reported on the deposition of Ir cluster arrays on Gr/Ir(111).[69] Ir is deposited on Gr/Ir(111) by resistive evaporation from a Knudsen cell. The size of the resulting metal clusters is governed by the dimensions of the Moiré unit cell. Additionally, since the clusters are formed preferentially in a certain area of the Moiré unit cell, ordering of the clusters in a regular array was observed. Since then, the

fabrication of similar nanocluster arrays consisting of a number of different metals has been reported on several different substrates.[70-75]

In this thesis, graphene-supported nanocluster arrays on a Rh(111) single crystal were investigated by high resolution XPS (HR-XPS). The fundamentals of XPS are explained in Chapter 2.1. Subsequently, background information on graphene on lattice-mismatched substrates, especially Rh(111), is reviewed in Chapter 2.2. The data on sulfur and sulfur oxides, SO_x (x = 1 – 4), on Pd(100) are discussed in Chapter 3. This part was a continuation of my master thesis. First the adsorption and reaction of SO_2 on the clean and oxygen precovered Pd(100) surface are shown in Chapter 3.1. Secondly the kinetics of the sulfur-oxidation are discussed in Chapter 3.2. The results on graphene supported nanocluster arrays on Rh(111) are presented in Chapter 4. First, further insigths into the properties and preparation of Graphene on Rh(111) are discussed in Chapter 4.1. Furthermore, the growth and thermal stability of Pd cluster arrays, as well as the adsorption of CO on these arrays are explored in Chapter 4.2. Finally, three important aspects of the reactivity of Pt nanocluster arrays are presented in Chapter 4.3: CO adsorption, CO oxidation, and SO_2 adsorption and reaction. Finally, the main results are summarized in Chapter 5.

2 Fundamentals

2.1 Synchrotron-based X-ray photoelectron spectroscopy

Basic principles of XPS [26]

X-ray photoelectron spectroscopy is based on the photoelectric effect.[76-77] Upon irradiation of a sample with the work function Φ_S with photons of the excitation energy $h\nu$, electrons with the binding energy E_B are excited and leave the sample with the kinetic energy E_{kin} relative to the vacuum level of the sample:

$$E_{kin} = h \cdot \nu - E_B - \Phi_S.$$

Depending on the excitation energy, one distinguishes between ultraviolet photo-electron spectroscopy (UPS) and X-ray photoelectron spectroscopy (XPS). Electrons from the valence levels are excited by radiation energies ranging from 5 to 100 eV in UPS experiments, while the higher-energy radiation used in XPS (> 100 eV) is sufficient to excite electrons from the core levels. For solid state measurements, the Fermi level, E_F, is usually used as reference. The potential difference between Fermi level and vacuum level of the sample corresponds to the work function, Φ_S, of the solid state material. When investigating a conducting sample, sample and analyzer are electrically connected, such that their E_F align. The electrons ejected from the sample are analyzed for their kinetic energy E_{kin}. If the work function of the analyzer Φ_A and the excitation energy $h\nu$ are known, the binding energy E_B of the excited core level electrons is easily calculated:

$$E_{kin} = h \cdot \nu - E_B - (\Phi_S - \Phi_A) - \Phi_A.$$

The binding energy E_B is characteristic for different elements. Due to spin-orbit coupling, s core levels lead to one peak in XP spectra, while p, d and f core levels are characterized by two peaks of a fixed intensity ratio. Because the cross section does not depend on the local chemical environment of the emitting atom, XPS can give quantitative information on the chemical composition of a sample or the coverage of a surface with adsorbates. Although the core electrons are not directly involved in chemical bonding, their exact binding energy depends on the chemical environment of the emitting atom. This "chemical shift" provides informa-tion on binding partners, oxidation state, and adsorption sites of surface species. Chemical shifts can generally be divided into initial and final state effects. In the case of an initial state effect the binding energy is changed by the chemical

surrounding of the atom before the interaction with light. Partial charges at the emitting atom lead to attractive or repulsive coulomb interaction with the electrons and therefore induce higher or lower binding energies, respectively. In this way, the binding energy of core level electrons is significantly influenced by the oxidation state of a specific atom as well as the electronegativity of its bonding partners. Final state effects result from energy made available in the relaxation of the remaining electrons after the interaction with light, i.e. after the electron is ejected from its original core level. The excitation of a second electron into the valence band ("shake up") or complete removal from the atom ("shake off") are typical final state effects and result in distinct satellites at higher binding energies. Screening effects of the surrounding electrons are also important final state effects, because they highly influence the degree of interaction between emitted electron and generated core hole. Taking initial and final state effects into account, binding energy shifts are difficult to predict in a quantitative way. Therefore, it is often useful to calculate chemical shifts with DFT in order to gain a complete description and interpret experimental data.

The radiation necessary to excite electrons from solids is generated either by conventional X-ray tubes or by synchrotron radiation sources. Commercial X-ray tubes are typically operated with magnesium or aluminium anodes and are well-suited for laboratory applications. The advantages of synchrotron radiation sources are the high intensity and brilliance of the generated radiation as well as the possibility of varying the photon energy. The high intensity makes very short acquisition times for spectra possible and therefore enables time-resolved measurements. Individual adjustment of the excitation energy to each investigated core level can optimize both surface sensitivity and photoelectric cross section resulting in higher electron yields. Surface sensitivity is maximized for kinetic energies between 50 and 100 eV, because in this regime the mean free path is only three to five atomic layers. The small mean free path of the electrons leaving the surface makes XPS a very surface sensitive method, which is therefore well suited for the investigation of adsorbate layers on surfaces.

Experimental details and sample preparation

All XP measurements were performed at Beamline U49/2-PGM1 of Helmholtz-Zentrum Berlin in a transportable UHV apparatus consisting of two chambers.[78] The hemispherical electron energy analyzer Omicron EA 125 U7 HR and a quadrupole mass spectrometer (QMS) for residual gas analysis are situated in the

analysis chamber, which is also connected to the beamline and the three-stage supersonic molecular beam. The preparation chamber houses a sputter gun, LEED optics, and a quartz crystal microbalance (QCM). Several electron beam evaporators are mounted either opposite to the QCM in the preparation chamber for thickness calibration or directly in the analysis chamber to enable the recording of XP spectra during metal deposition. A Microcapillary array doser systems are connected to both preparation and analysis chamber. The background pressure is typically in the range of 10^{-10} mbar.

The samples are a cylindrical Pd(100) single crystal with 10 mm diameter and 2.0 mm thickness and a cylindrical Rh(111) single crystal with 10 mm diameter, 3.0 mm thickness, and an orientation accuracy of 0.1°, purchased at MaTeck. Two independent type K thermocouples spotwelded to the crystals are used to measure the sample temperature. Both crystals are cleaned by sputtering and annealing cycles. On the Pd sample, sulfur and carbon contaminations are removed by exposure to O_2 at 300 K, followed by heating to 970 K to desorb the excess oxygen. On the Rh sample carbon contaminations are removed by oxidation with $2 \cdot 10^{-6}$ mbar oxygen at 900 K and subsequent flashing to 1200 K to desorb oxygen. The final cleanliness of the respective sample is checked by XPS. A combination of liquid nitrogen cooling and resistive heating allow for sample temperatures between 100 and 1400 K. An additional filament is mounted in the back of both samples to perform linear heating ramps during XP measurements without a disturbing influence on the measurements. Such measurements are referred to as temperature programmed (TP-XPS) experiments in the following.[79-80] Propene, ethene, CO and oxygen were dosed with the supersonic molecular beam, and SO_2 and H_2S were dosed using the microcapillary array doser. All exposures are given in langmuirs (L, $1.33 \cdot 10^{-6}$ mbar $\cdot$ s). Atomic sulfur was deposited on the Pd(100) crystal by adsorption of H_2S at temperatures below 200 K and subsequent heating to 700 K to desorb hydrogen. Pt and Pd were deposited by electron beam evaporation.

Data acquisition and evaluation

Spectra were recorded either at normal emission (0°) or with an angle of 69° to the analyzer to allow for metal evaporation while performing XPS measurements. The diameter of the photon beam on the sample was roughly 125 μm. The aqcuisition time for a single spectrum is typically 10 s or less. All spectra are referenced to the Fermi level and a linear background is subtracted from each

spectrum. To account for fluctuations in the light intensity, spectra are normalized to the background of the first spectum of each experiment. The spectra are fitted with convolutions of Doniach-Šunjić functions and Gaussian functions.[81]

On the Pd(100) sample, the sulfur coverages were calibrated using a c(2 × 2) overlayer of S with a coverage of 0.5 ML, which was prepared by dosing H_2S onto the surface at 300 K, followed by heating to 550 K in order to desorb H_2, and subsequently cooling down to 300 K.[29, 82] This procedure was repeated until saturation was reached. All S 2p spectra used for the calibration were collected with a photon energy of 380 eV in order to minimize photoelectron diffraction effects. For the measurements on the graphene-supported nanoclusters on Rh(111) the carbon and oxygen coverages were calibrated using a reference structure of CO with a coverage of 0.75 ML.[32] The sulfur coverages were calibrated indirectly by comparing the amounts of adsorbed CO with and without sulfur present. Pd and Pt coverages were calibrated using the QCM. One ML thereby corresponds to one adsorbate atom or molecule per Pd or Rh surface atom, respectively.

2.2   Graphene on lattice mismatched substrates

Growth mechanism

Graphene is produced by a CVD process on the Rh(111) surface.[54, 59] In this work, ethene and propene were used as carbon precursors. At sufficient sample temperatures, the precursor is cracked into carbon fragments and hydrogen, which desorbs from the surface. A detailed STM study on Ir(111) revealed that substrate step edges play a decisive role for graphene nucleation during CVD.[62] Furthermore, the incorporation of carbon adspecies at the graphene edges is suggested as the rate limiting step. These findings are in agreement with electron reflectivity results for graphene growth on Ir(111) and Ru(0001), indicating the addition of carbon five rings as the rate determining step for graphene growth.[83-84] STM and DFT studies on Rh(111) suggest C_{21} and C_{24} clusters as likely nucleation sites for graphene growth during CVD.[85-86] Thus, it is possible to manipulate the number of defects in graphene by controlling the C_{21} cluster concentration. Consequently the defect density and average domain size depend strongly on the graphene growth parameters (see Chapter 4.1.1).

<u>Morphology</u>

The morphology and electronic structure of graphene on a metal substrate strong-ly depend on the specific chemical interactions and the lattice mismatch between graphene and the respective metal surface.[54-55, 59, 87] The lattice mismatch of roughly 10 % between Gr and the Rh(111) surface results in a Moiré super-structure consisting of 12 x 12 Gr over 11 x 11 Rh unit cells with a periodicity of 2.9 nm. The resulting complex corrugation pattern has been described in detail by STM and AFM measurements as well as DFT calculations.[64-65] In those regions of the supercell, where a carbon ring is centered over a bridge position, hybridization between Gr and Rh 4d states occurs, leading to a carbon-Rh distance of less than 2.3 Å. In contrast, in those regions where carbon rings are centered on top of a Rh atom, the interaction between Rh and Gr is weak and the carbon-metal distance is more than 3 Å.[64] XP spectra of graphene on different lattice mis-matched substrates are shown in Ref. 59.
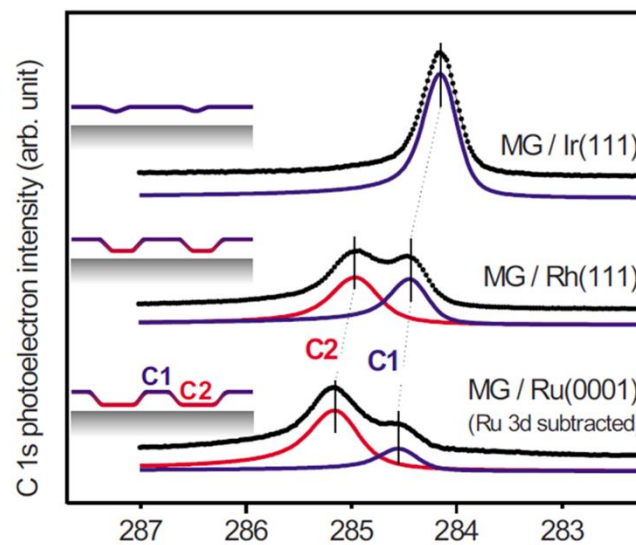

Figure 2.1: High-resolution XP spectra of monolayer graphene (MG) on different lattice mismatched substrates. The excitation energy was 400 eV. The Ru 3d signal was subtracted from the Ru(0001) data. Adapted from Ref. 59.

Graphene on Ir(111) exhibits one C 1s signal at 283.97 eV, while two graphene signals are observed for Gr on Rh(111) and Ru(0001). NEXAFS and angle resolved UPS data reveal that graphene is coupled weakly to the Ir sub-strate.[59, 88] Thus the graphene signals at lower binding energies from Gr on Rh and Ru at 284.41 and 284.52 eV, respectively, are assigned to areas of the graphene layers that are weakly coupled to the respective substrate. Accordingly, the signals at higher binding energies, 284.94 eV for Gr/Rh and 285.12 eV for

Gr/Ru, are assigned to areas of the graphene layer that interact strongly with the substrate. For Gr/Ru(0001), the signal of strongly coupled graphene is significantly higher than the one of weakly coupled graphene and both graphene signals appear at higher binding energies than for Gr/Rh(111). Else, the signals of strongly and weakly coupled Gr on Rh(111) exhibit roughly the same height. Therefore, Gr on Rh(111) is considered as an intermediate case between strong and weak coupling.[59, 64] Depending on the interaction strength with the Rh substrate, carbon atoms from different positions in the graphene layer exhibit varying chemical shifts in the C 1s core level. The superposition of peaks from carbon atoms with different interaction strengths leads to two separated C 1s signals from strongly and weakly coupled graphene.[59, 89]

<u>Characterization of Gr/Rh(111)</u>

The distinct LEED pattern originating from the 11 x 12 Moiré supercell is shown in Figure 2.2a. Note that this characteristic LEED pattern[59] was found only for graphene layers with extended domains and a low defect density (see Chapter 4.1). For graphene layers containing smaller domains and more defects, diffuse circles were observed instead of clearly resolved spots. The valence band of Gr/Rh(111) is shown in Figure 2.2b. It was recorded with 100 eV excitation energy at normal emission, and therefore corresponds to data at the Γ-point. In comparison to weakly coupled graphene, the π and σ bands of graphene are shifted towards higher binding energies due to the coupling with the Rh substrate.[57, 90-91] Similar valence band spectra were observed for all investigated graphene layers, independent of the defect density.
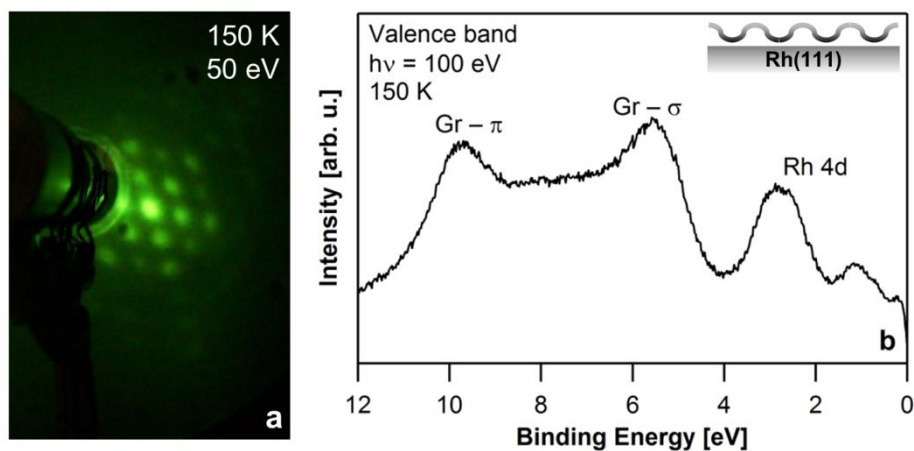

Figure 2.2: a) LEED pattern (0,0 spot) of a low defect density graphene layer at 150 K, recorded with an electron energy of 50 eV. b) Valence band of Gr/Rh(111) at 150 K. The spectrum was recorded normal emission and therefore corresponds to the Γ-point.

3 Sulfur and its oxides on Pd(100)

3.1 SO₂ Adsorption and reaction on clean and oxygen precovered Pd [P1]

The adsorption and reaction of SO₂ on Pd(100) was investigated in detail by HR-XPS. Relative binding energy shifts predicted by DFT calculations support the assignment of the surface species observed in XPS. In the following, S 2p binding energies will be given in the form S $2p_{3/2}$ (S $2p_{1/2}$) eV.
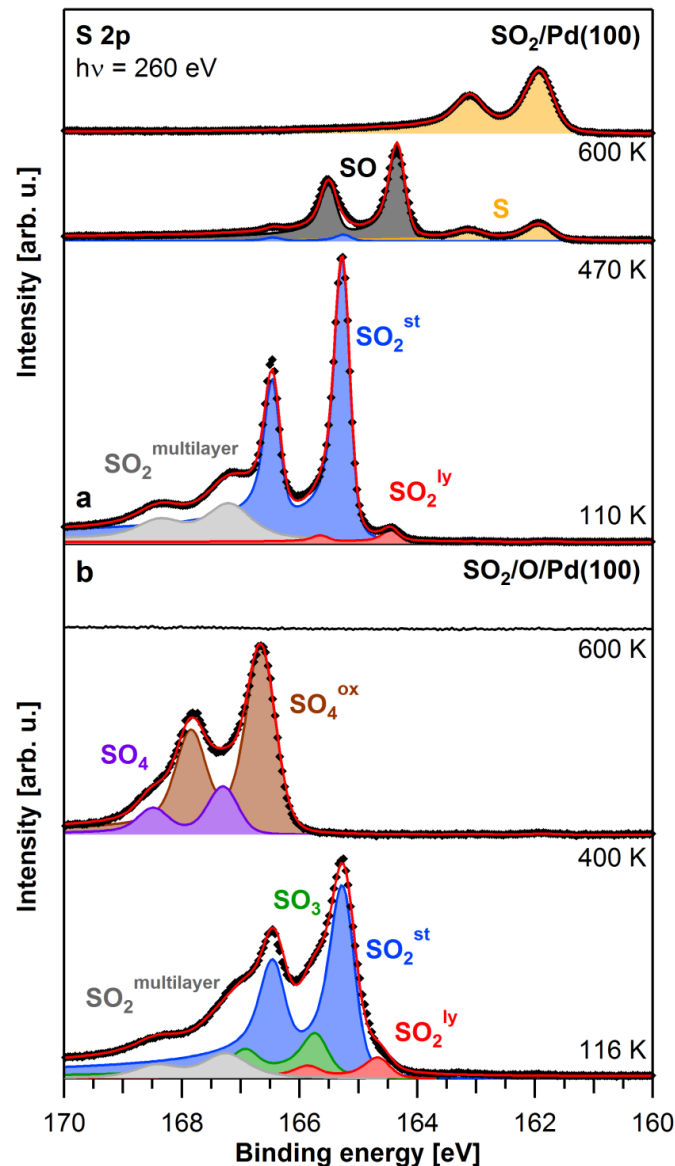

Figure 3.1: Selected S 2p spectra of the SO₂ adsorption and reaction on Pd(100).
a) Clean Pd(100) surface. Bottom: spectrum after adsorption of 0.9 L SO₂ at 110 K. Top: spectra recorded during TP-XPS at 470 and 600 K. b) Bottom: 0.25 L SO₂ adsorbed on Pd(100) precovered with 0.30 ML oxygen. Top: spectra recorded during TP-XPS at 400 and 600 K.TP-XPS experiments were performed with a linear heating rate of 0.5 K/s.

The S 2p core level spectrum after adsorption of 0.9 L SO_2 on the clean Pd(100) surface at 110 K is shown in the bottom part of Figure 3.1a. The spectrum consists of two narrow S 2p doublets at 165.3 (166.5) and 164.5 (165.7) eV, and a broader doublet at 167.0 (168.2) eV. The two narrow doublets are assigned to SO_2 adsorbed in η^2 (standing, SO_2^{st}) and η^3 (lying, SO_2^{ly}) geometry, respectively. The SO_2^{st} signal (blue) is much more intense than the SO_2^{ly} signal (red), since the standing adsorption geometry is energetically favorable. The broader doublet stems from SO_2 multilayers (gray). After SO_2 adsorption, a linear heating rate of 0.5 K/s was applied to investigate the thermal reaction behavior. Two selected spectra during the TP-XPS experiment recorded at 470 and 600 K are displayed in the upper part of Figure 3.1a. At 470 K, the multilayer and SO_2^{ly} signals have vanished and only a minor amount of SO_2^{st} remains on the surface. Two new doublets at 164.3 (165.5) and 161.9 (163.1) eV stem from SO (black) and atomic sulfur (orange), respectively. The assignment of the doublet at 164.3 (165.5) eV to SO is indicated by a number of considerations including the DFT results and is discussed in detail in reference [P1]. As the overall signal intensity is reduced in comparison to the spectrum at 110 K, SO_2 partly desorbed from the surface and partly reacted to SO and S. From the amount of oxygen left on the surface after the reaction, it is concluded that sulfur mainly desorbs in the form of SO_3 rather than SO_2. At 600 K (topmost spectrum in Figure 3.1a) only atomic sulfur remains on the surface. In conlusion, the stepwise reduction of SO_2 to first SO and finally atomic sulfur was observed for the thermal reaction of SO_2 on the clean Pd(100) surface.

The spectrum of 0.25 L SO_2 adsorbed on Pd(100) precovered with 0.30 ML oxygen at 116 K is shown in Figure 3.1b. In analogy to the clean Pd(100) surface, two doublets from SO_2 molecules in standing and lying adsorption geometry are observed at 165.3 (166.5) eV and 164.6 (165.8) eV, respectively. Due to lateral interactions with the preadsorbed oxygen, the SO_2 signals are broadened by 50 % in comparison to the clean surface and the SO_2^{ly} signal is shifted slightly to higher binding energies. Again, SO_2^{st} is the majority species and SO_2^{ly} is only occupied to a small extent. The additional signal at 165.8 (167.0) eV is assigned to SO_3 (green), which is formed upon adsorption due to an Eley–Rideal mechanism. As for the clean Pd(100) surface a multilayer signal is observed at 167.1 (168.3) eV.
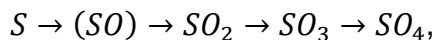
After adsorption, a TP-XPS experiment was performed to investigate the thermal reaction behavior. Upon heating, the SO_2 signals vanish while the intensity of SO_3 increases. At 250 K, the intensity of SO_3 reaches its maximum

and decreases thereafter. Between 200 and 350 K, two additional signals at 166.8 (168.0) and 167.4 (168.6) eV evolve. At 400 K (middle spectrum in Figure 3.1b), these two signals are the only ones left. In agreement with the DFT results, the signal at 166.8 (168.0) eV is assigned to SO_4 adsorbed in proximity of oxygen adatoms (SO_4^{ox}, brown), while the signal at 167.4 (168.6) eV corresponds to SO_4 bound remote from any oxygen (SO_4, purple). Upon further heating, SO_4 decomposes and desorbs, leaving only oxygen on the surface. The spectrum recorded at 600 K (topmost spectrum in Figure 3.1b) shows that no sulfur-containing species is left on the surface, in contrast to the case of the clean Pd(100) surface.

In conclusion a clear assignment of the observed SO_x (x= 0 − 4) species on clean and oxygen covered Pd(100) was made by comparison of the XP data to DFT results. The thermal reaction behavior of SO_2 on the clean surface is contrary to that on oxygen-precovered Pd(100). In the first case a stepwise reduction to SO and finally atomic sulfur was observed, while in the latter case the stepwise oxidation to SO_3 and SO_4 was found. As SO_4 decomposes and desorbs, the oxygen-precovered surface is free from sulfur residues at 600 K. This finding indicates that sulfur poisoning in Pd catalysts can be avoided by working under oxygen-rich conditions.

3.2   Oxidation of atomic sulfur [P2]

To further investigate the removal of atomic sulfur from Pd(100), 0.034 ML sulfur were coadsorbed with 0.23 ML of oxygen at 140 K. Subsequently, a TP-XPS experiment with a linear heating rate of 0.5 K/s was conducted. Upon heating, small amounts of SO_2 and SO_3 are observed until 300 and 450 K, respectively. In this experiment, only the more stable SO_2^{st} is observed. At 250 K, a SO_4 doublet evolves and steadily increases until its maximum is reached at 500 K. Due to the high oxygen coverage in comparison to the coadsorbed amount of sulfur, the majority of adsorbed SO_4 interacts with an oxygen adatom. Thus the binding energy of the observed SO_4 doublet is considerably closer to the binding energy of the SO_4^{ox} species than the SO_4 species observed in the earlier study ([P1], see Chapter 3.1). At higher temperatures the SO_4 coverage decreases quickly until SO_4 has vanished completely until 560 K. The atomic sulfur coverage stays constant until 430 K and subsequently decreases until no sulfur-containing species is left on the surface at 600 K. The subsequent formation of surface species implies the following stepwise oxidation mechanism:

$$S \rightarrow (SO) \rightarrow SO_2 \rightarrow SO_3 \rightarrow SO_4,$$

with the rate limiting step being the oxidation of atomic sulfur to SO. Since the reaction intermediate SO is not observed in XP spectra, the succeeding oxidation to SO_2 occurs rapidly. This mechanism is in excellent agreement with reaction energy profiles obtained from DFT calculations. At temperatures above 450 K, SO_4 decomposes and desorbs in the form of SO_3 or SO_2 ([P1], see Chapter 3.1).

To gain insight into the reaction kinetics, the temperature range from 400 to 500 K was chosen to record series of isothermal oxidation experiments. The quantitative analysis of the oxidation experiment at 450 K with an oxygen pressure of $2.1 \cdot 10^{-6}$ mbar is shown in Figure 3.2. The coverages of SO_2 and SO_3 are not shown, because their amounts are negligible in comparison to sulfur and SO_4. The coverages of the SO_4 and SO_4^{ox} species are summed up for clarity.
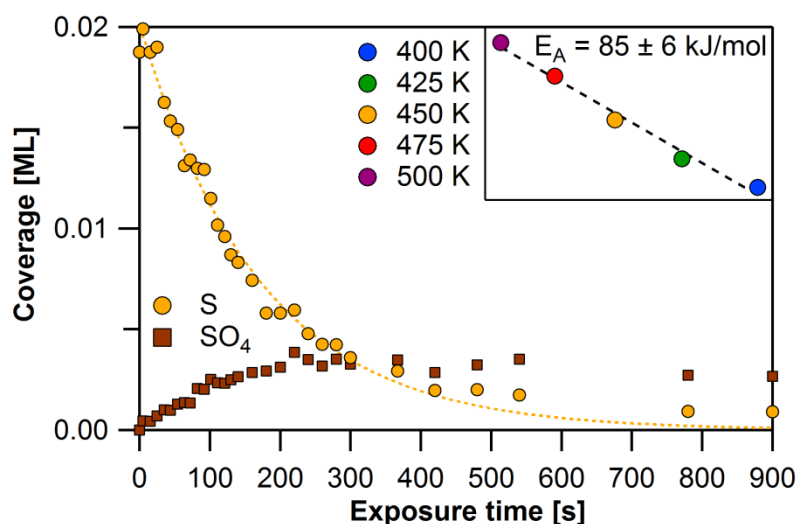

Figure 3.2: Isothermal oxidation of atomic sulfur on Pd(100) at 450 K with an O_2 pressure of $2.1 \cdot 10^{-6}$ mbar. The sulfur coverage is fitted with an exponential function (dashed orange line) to obtain the reaction constant. Inset: Arrhenius plot (ln[k] versus 1/T) showing reaction constants of several measurements at different temperatures. The activation energy determined from this plot is 85 ± 6 kJ/mol.

With beginning oxygen exposure, the coverage of SO_4 (brown squares) starts to increase. It saturates around 200 s and slighty decreases until the end of the experiment at 900 s. The sulfur coverage (orange circles) decays steadily upon oxygen exposure and is fitted with an exponential function (dashed orange line). The good agreement with the fit shows, that the rate limiting step of the reaction follows a pseudo-first-order rate law. The reaction constant, k_{obs} is determined from the fit. The inset of Figure 3.2 shows the reaction constants from the

complete measurement series between 400 and 500 K in an Arrhenius plot. From this Arrhenius plot an activation energy of 85 ± 6 kJ/mol is determined. This energy is higher than the value of 51 ± 4 kJ/mol found on Pt(111),[40] suggesting that sulfur contaminations are more easily removed from Pt than Pd catalysts.

In conclusion, the oxidation of atomic sulfur on Pd(100) was investigated in detail by a temperature programmed reaction experiment and a series of isothermal oxidation experiments. The oxidation proceeds stepwise from atomic sulfur to SO, SO_2, SO_3 and finally SO_4. The rate limiting step thereby is the formation of SO, which is not observed as an intermediate by XPS. Subsequently, SO_4 decomposes and desorbs in the form of SO_2 or SO_3. The proposed mechanism is in excellent agreement with DFT results. The isothermal oxidation reaction follows pseudo-first order kinetics. By Arrhenius analysis the activation energy of the rate limiting step is determined to 85 ± 6 kJ/mol.

4 Graphene-supported nanocluster arrays on Rh(111)

4.1 Graphene on Rh(111) – new insights

4.1.1 <u>Growth parameters</u> [P3]

Graphene was grown on Rh(111) employing a CVD process.[54-55] To find the optimum conditions for the production of defect-free graphene, a wide range of different preparation parameters including growth temperature and precursor pressure was explored. To grow a graphene layer, the Rh(111) sample is heated resistively to the desired growth temperature and a carbon precursor, in this case propene, is dosed onto the sample. Propene is dosed either directly onto the sample with the supersonic molecular beam, creating local pressures of up to $1 \cdot 10^{-5}$ mbar, or the chamber is backfilled with propene by inserting a flag into the beam path. The growth of graphene is monitored by recording XP spectra in the C 1s region during propene exposure. Two graphene-related signals at 285.2 and 284.6 eV evolve simultaneously with increasing propene exposure. The peaks stem from carbon atoms in the graphene lattice interacting strongly and weakly with the Rh substrate and are referred to as C^1 and C^2 respectively in the follo-wing.[55, 59, 64-65] Throughout the entire growth process, the ratio of $C^1 : C^2$ is constant within 15 %. As the Rh surface is covered with a monolayer of graphene, the carbon coverage saturates, because propene cannot be cracked on the graphene. After the surface is saturated with graphene, the propene exposure is stopped and the sample is allowed to cool down. During cooling, a narrowing of the graphene signals is observed, which is larger than expected from the tempe-rature-induced narrowing of the Fermi edge. Furthermore, the narrowing is 58 % greater for the weakly bound C^2 than for the strongly bound C^1. The decrease in full width at half maximum (fwhm) is attributed to the fact that at lower tempera-tures less vibrations of the graphene layer are excited and thus the local environ-ment is more defined, leading to a smaller linewidth. This effect is smaller for carbon atoms that are bound more strongly to the Rh substrate. Therefore, the observed decrease in linewidth is not as pronounced for the strongly bound as for the weakly bound carbon atoms. During cooling, the ratio between the two carbon species decreases, indicating that at lower temperatures more carbon atoms are at a larger distance from the Rh surface.

Spectra after cooling down to 150 K of two different graphene layers are shown in Figure 4.1a and b. Both layers were prepared at 920 K, but at different

propene pressures. The graphene layer in Figure 4.1a was prepared at $2 \cdot 10^{-8}$ mbar by backfilling the chamber with propene. In this case, the graphene signals evolve slowly over time and saturate after around 90 min. The spectrum exhibits the two characteristic graphene signals, C^1 and C^2, at 285.2 and 284.6 eV, with fwhms of 530 and 410 meV, respectively.[59] Furthermore, the layer shows a distinct LEED pattern[59] due to the Moiré superstructure of graphene on Rh(111) and a valence band in good agreement with literature.[92] The small linewidth in the C 1s region, the distinct LEED pattern, and the slow oxidation behavior (see Chapter 4.1.2) indicate a low defect density of this graphene layer. All graphene layers that were used for the fabrication of graphene-supported nanoclusters arrays in the following chapters were prepared with these CVD parameters to ensure a low defect density.
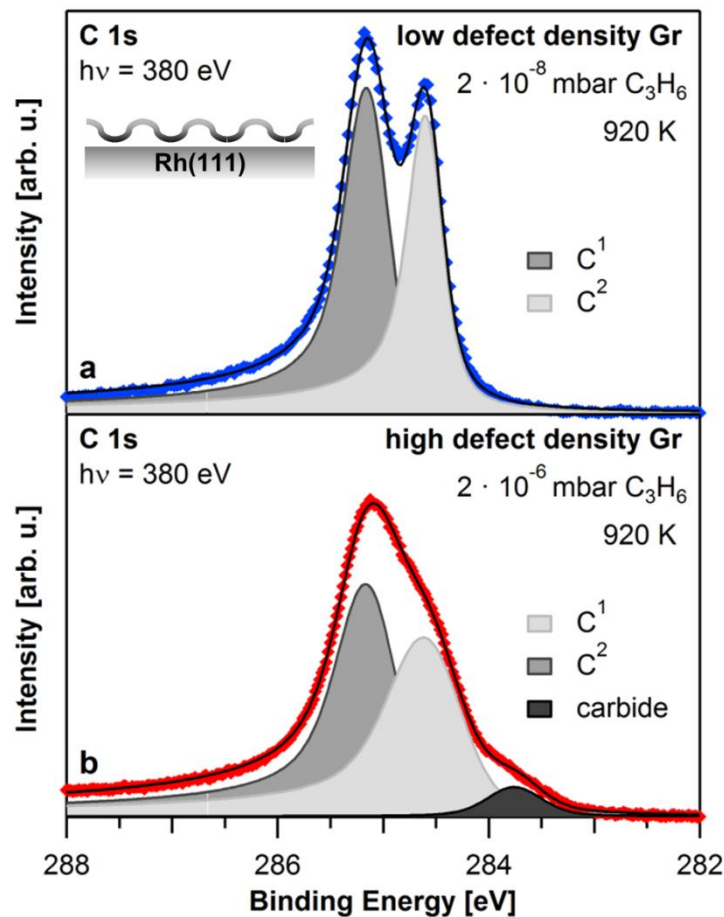

Figure 4.1: Growth of graphene on Rh(111). a) Fit of a C 1s spectrum of a low defect density graphene layer grown at 920 K with a propene pressure of $2 \cdot 10^{-8}$ mbar on Rh(111). b) Fit of a C 1s spectrum of a high defect density graphene layer grown at 920 K with a propene pressure of $2 \cdot 10^{-6}$ mbar on Rh(111). Both spectra in a) and b) were recorded at 150 K.

The graphene layer in Figure 4.1b was prepared at $2 \cdot 10^{-6}$ mbar by hitting the sample directly with the molecular beam. For this precursor pressure, the graphene signals evolve quickly and the C 1s intensity is saturated after 5 min of propene exposure. The two graphene signals at 285.2 and 284.6 eV are much broader than those of the layer in Figure 4.1a prepared with a lower propene pressure. The fwhms of the strongly and weakly coupled signals are 730 and 870 meV, respectively. The spectrum exhibits an additional shoulder at 283.8 eV, which is assigned to carbidic carbon due to defects in the graphene layer. The carbidic carbon signal comprises 6 % of the total C 1s signal intensity. The LEED pattern of this graphene layer showed diffuse circles instead of distinct Moiré spots. However, no significant difference of the valence band in comparison to the layer in Figure 4.1a was observed. The unchanged valence band proves that the layer prepared with the higher propene pressure is also graphene. However, the fast growth procedure leads to a multitude of different domains, with defects at the domain boundaries. The high defect density of graphene layers prepared at higher precursor pressures is also confirmed by oxidation experiments (see Chapter 4.1.2).

In addition to the precursor pressure, also the influence of the sample temperature on graphene growth was tested. For temperatures lower than 920 K, a broadening of the graphene signals and an increase of the carbidic carbon signal was observed, similar to the case of higher propene pressure. This is due to the fact that at lower temperatures the lifetime of C_{21} carbon clusters increases, leading to a higher number of nucleation sites for graphene.[85] Increasing the temperature and thereby minimizing the number of nucleation sites leads to less, more extended domains and thus to less defects. In contrast, if the temperature is significantly higher than 920 K, the solubility of carbon in Rh increases and a propene pressure of $2 \cdot 10^{-8}$ is not sufficient to achieve saturation of the surface with carbon. Therefore, the growth process at 1000 K had to be performed with a higher propene pressure, again leading to more domain boundaries and a higher defect density.

In conclusion, a wide parameter range was explored for the growth of graphene on Rh(111). The defect density and quality of differently prepared graphene layers was checked with XPS, UPS and LEED. A sample temperature of 920 K and a propene pressure of $2 \cdot 10^{-8}$ mbar, allowing for a slow growth process, proved as the optimum to obtain graphene layers with extended domains and few defects.

4.1.2   Oxidation of graphene [P3]

The oxidation of different graphene layers was investigated *in situ* by dosing oxygen directly onto the sample with the molecular beam, while the sample is heated resistively. During O_2 exposure, the two graphene signals vanish simultaneously and no other carbon or carbon-oxygen species are observed as reaction intermediates. These findings suggest that graphene is etched by oxygen and directly desorbs as CO or possibly CO_2. The graphene coverages of a low and a high defect density graphene layer (blue and red diamonds, respectively) during exposure to $2 \cdot 10^{-6}$ mbar oxygen at 700 K are given in Figure 4.2. Both curves exhibit a characteristic S-shape and are fitted with sigmoidal functions (dashed black lines). The sigmoidal kinetics can be explained as following: in the beginning of oxygen exposure, oxygen only adsorbs at defect sites and domain boundaries of graphene. In this induction period, graphene is slowly etched away starting from defects and the reaction rate only depends on the number of defects in the graphene layer.
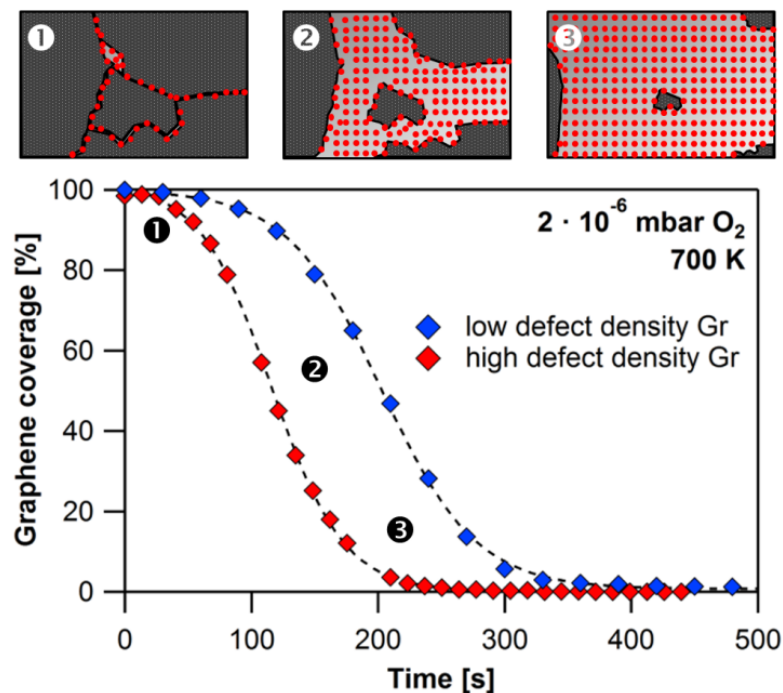

Figure 4.2: Graphene coverage in percent during oxidation of graphene at 700 K with $2 \cdot 10^{-6}$ mbar O_2; blue diamonds: low defect density graphene; red diamonds: high defect density graphene. The different stages of oxidation are shown schematically in the top.

This relationship is clearly seen in Figure 4.2: the induction period for the low defect density graphene layer (blue) is significantly longer than for the high defect density graphene layer (red). As graphene is etched away, an increasing

part of the Rh surface becomes available for the adsorption of oxygen and thus the reaction accelerates. In this regime, the reaction rate depends on both the number of free adsorption sites (fraction of graphene already etched from the surface) and the carbon coverage (fraction of the surface still covered with graphene). When most of the graphene layer is etched away, the reaction slows down again. Since oxygen is supplied in excess from the gas phase, in this regime the reaction rate depends only on the graphene coverage. Therefore the last part of the reaction follows pseudo-first-order kinetics and equals an exponential decay.[93] The three different regimes are also shown schematically in the top of Figure 4.2. The oxidation of low and high defect density graphene was investigated in the temperature range between 700 and 1000 K. For the high defect density graphene very slow etching was also observed at 600 K. In general, the reaction is significantly faster for the high defect density graphene, as it starts at the defects. As expected, the slope of the intermediate reaction regime is temperature dependent. However, the induction period for graphene layers prepared under the same conditions somewhat varies due to the random distribution of domain boundaries, which complicates a detailed kinetic analysis of the data.

In conclusion, the oxidation of graphene layers with varying defect density was investigated in a wide temperature range. The reaction proceeds in three subsequent regimes: the oxidation starts with an induction period, which is determined by the number of defects in the graphene layer. Afterwards the reaction accelerates and is governed by both the free Rh surface area and the remaining graphene coverage. Finally, the reaction rate depends only on the remaining carbon coverage and follows pseudo-first-order kinetics.

4.2 Pd nanocluster arrays – fabrication and properties

4.2.1 Fabrication [P4]

Graphene-supported Pd nanocluster arrays were investigated by a combination of HR-XPS and STM measurements. A low defect density graphene layer was grown by CVD of $2 \cdot 10^{-8}$ mbar propene at 920 K and allowed to cool down to 150 K. Subsequently, Pd nanoclusters were deposited by electron beam evaporation, while recording Pd 3d core level spectra. Upon deposition a broad asymmetric signal evolves, which is fitted with three components in agreement with literature: the Pd bulk signal at 335.1 eV and two surface signals at 335.5 and

334.9 eV.[94] With increasing Pd coverage, the ratio of bulk to surface intensity increases quickly until a coverage of 0.3 ML Pd. At coverages higher than 0.3 ML, the bulk-to-surface-ratio saturates, indicating that, after a critical cluster size is reached, the cluster density increases rather than the average cluster size. These findings indicate a template-assisted cluster-by-cluster growth mode, as was also found for several different graphene-supported nanocluster systems.[69-70, 72]
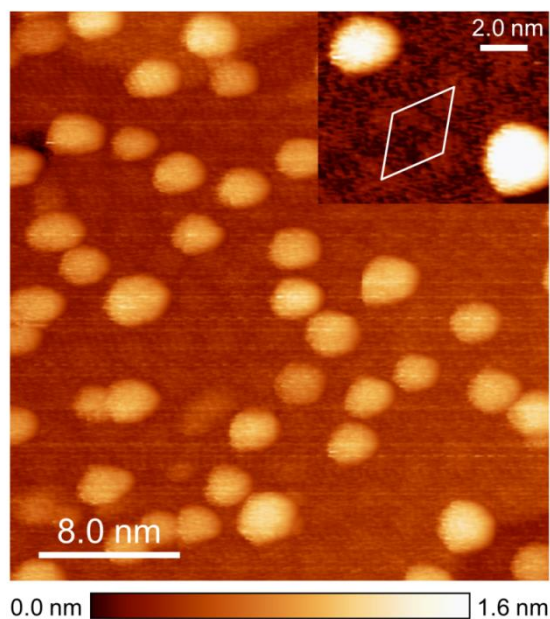

Figure 4.3: STM micrograph of Pd nanoclusters deposited on Gr/Rh(111) at room temperature. The inset shows the cluster size and position in relation to the dimensions of the Moiré unit cell (indicted by a white rhombus). The average cluster height is 6.6 ± 1.0 Å, corresponding to roughly 3 atomic layers and the average cluster diameter is 3.0 ± 0.3 nm.

To obtain more detailed information about the size and distribution of the Pd nanoclusters, additional STM measurements were performed. The same Rh(111) crystal and similar CVD parameters as in the XPS experiments were used to prepare the graphene layer. However, since there was no possibility for liquid nitrogen cooling in the STM apparatus, the Pd clusters were deposited at room temperature. An STM image of Pd nanoclusters deposited on Gr/Rh(111) is shown in Figure 4.3. The Pd particles exhibit a narrow size distribution. The average cluster height is 6.6 ± 1.0 Å, corresponding to roughly 3 atomic layers and the average cluster diameter is 3.0 ± 0.3 nm. From the inset of Figure 4.3 it is clearly seen that the size and position of the clusters is governed by the dimensions of the Moiré unit cell (2.9 ± 0.05 nm), as expected for a template-assisted growth process.

In conclusion, the fabrication of graphene-supported Pd nanoclusters was monitored by HR-XPS and STM measurements. The saturating bulk-to-surface-ratio as well as the fact that the cluster size is governed by the Moiré super-structure, indicate a template-assisted cluster-by-cluster growth mode. The average cluster height is three atomic layers and the average cluster size is 3 nm for clusters deposited at room temperature.

4.2.2 Thermal stability [P4]

To explore the thermal stability of the graphene-supported Pd nanoclusters, cluster samples were annealed stepwise and C 1s, Rh 3d and Pd 3d spectra were recorded after each heating step. The signal intensities for a 0.7 ML Pd sample are shown in Figure 4.4.
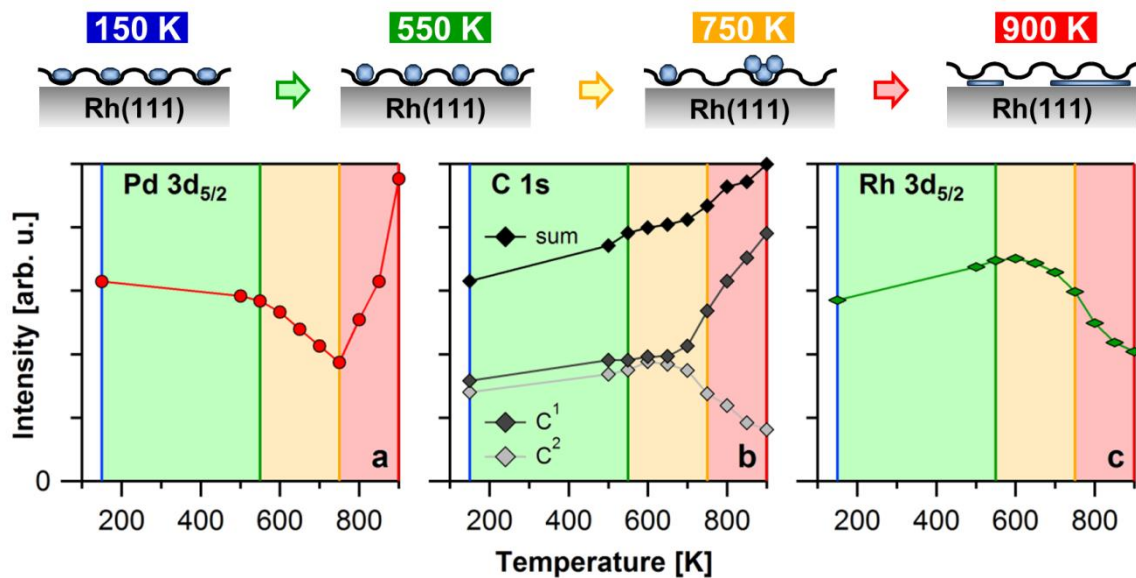

Figure 4.4: Thermal stability of Pd nanoclusters on Gr/Rh(111). a) Pd 3d intensity, b) C 1s intensity, and c) Rh 3d intensity during stepwise heating of a 0.7 ML Pd/Gr/Rh(111) nanocluster sample. The processes occuring in the three temperature regimes (restructuring, agglomeration, intercalation) are shown schematically in the top.

From analysis of the signal intensities it is possible to distinguish three temperature regimes. Until 550 K (green) the C 1s and Rh 3d intensities (Figure 4.4b and c) increase while the Pd 3d intensity in Figure 4.4a decreases slightly. This behavior is explained by restructuring of the nanoclusters towards a more threedimensional shape. The underlying graphene and rhodium signals are less attenuated, while accumulation of Pd layers leads to increased self damping of the metal signals. This model is also in agreement with STM data showing that number and distribution of the clusters is constant upon annealing up to 420 K.

This temperature range is well suited for the performance of adsorption and reaction experiments on the metal clusters, due to the stability of the particles. Between 550 and 750 K (yellow), the Pd 3d intensity decreases more strongly, while the C 1s and Rh 3d intensities stay almost constant until 700 K. These findings are attributed to agglomeration of the Pd clusters. At higher temperatures the metal clusters become more mobile and merge into larger agglomerates.[70] This leads to enhanced self damping of the Pd signal. The net effect on the underlying graphene and rhodium substrates is zero, since the areas that become Pd-free and the areas that are more attenuated cancel each other out. Finally, upon annealing to 900 K (red), the Pd 3d intensity increases up to 151 % of its original value, while the Rh 3d intensity decreases abruptly. Simultaneously, the C 1s intensity of strongly bound graphene decreases, while the intensity of weakly bound graphene increases. These findings are strong indicators for the intercalation of Pd between the graphene layer and the Rh substrate. After intercalation, graphene is the topmost layer; therefore, the total C 1s intensity increases. Furthermore, most of the graphene is coupled to Pd, which shows a weak interaction with graphene,[95] instead of Rh, leading to a shift of the binding energy in the C 1s region. As Pd forms a flat layer on the Rh, the attenuation of the Rh substrate is more pronounced. At the same time, the self-damping of the Pd layers is lifted. Therefore the Pd 3d intensity increases strongly.

In conclusion, three temperature regimes were found for the thermal stability of graphene-supported Pd nanoclusters. The clusters undergo slight restructuring towards a more threedimensional shape until 550 K. The stability of the cluster density in this temperature range was also confirmed by STM measurements. Up to 750 K the Pd clusters merge into larger agglomerates, and until 900 K Pd intercalates between graphene and Rh. The stability of the metal clusters between 150 and 550 K makes this temperature range well suited for conducting of adsorption and reaction experiments.

4.2.3   CO adsorption [P5]

To further investigate the properties of graphene-supported Pd nanocluster arrays, the adsorption of CO on varying amounts of Pd deposited on Gr/Rh(111) was investigated by HR-XPS. Upon CO exposure, in addition to the characteristic graphene signals at 285.1 and 284.5 eV in the C 1s region, an asymmetric signal at 285.9 eV evolves. With increasing exposure the CO-induced signal becomes broader and more asymmetric, and shifts to higher binding energies by 170 meV.

Due to the changing fwhm and asymmetry it was not possible to fit the C 1s spectra satisfyingly with only one CO contribution. Instead two CO peaks with constant fitting parameters were employed. The fit of the saturated C 1s spectrum of CO adsorbed on 0.7 ML Pd is shown in Figure 4.5a.
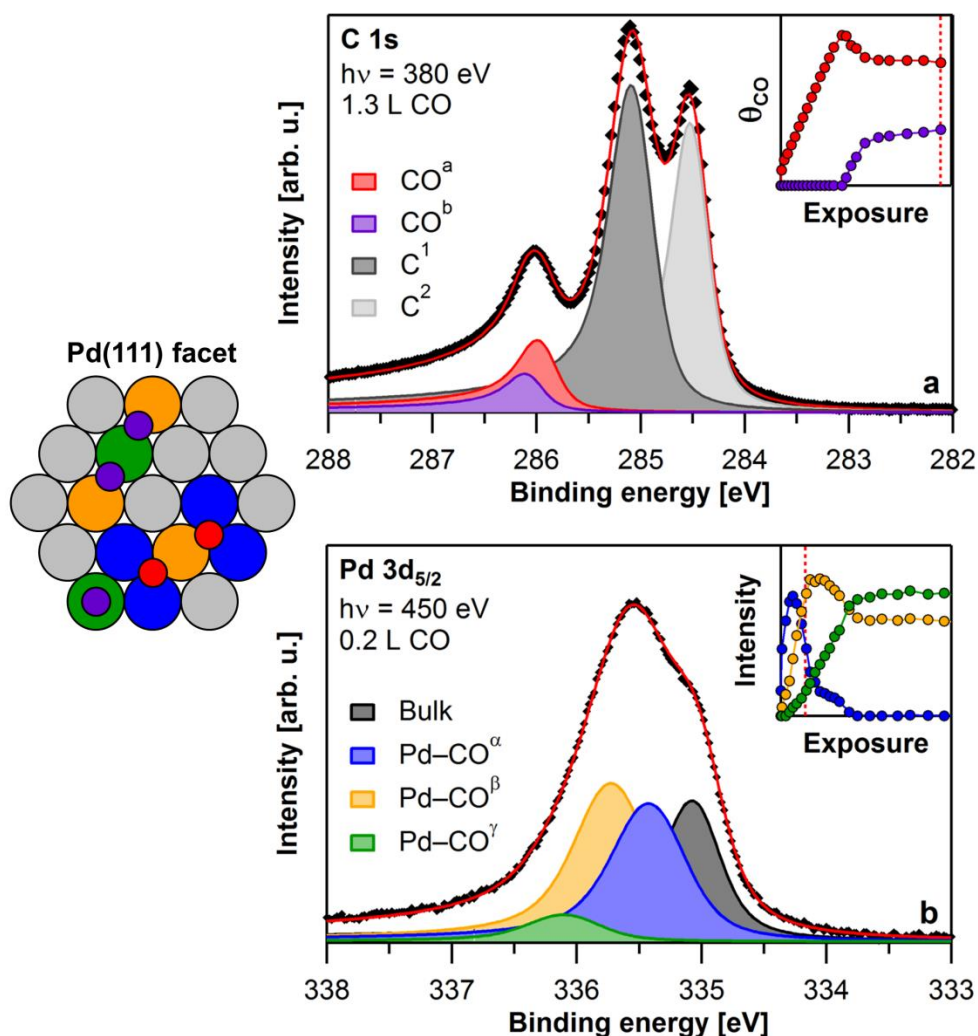

Figure 4.5: Adsorption of CO on 0.7 ML Pd nanoclusters on Gr/Rh(111) at 150 K. a) Fit of the saturated C 1s spectrum, recorded after exposure to 1.3 L of CO. Inset: partial CO coverage versus CO exposure as obtained from fitting, 1.3 L is marked with a vertical line. b) Fit of an intermediate Pd 3d$_{5/2}$ spectrum, recorded after exposure to 0.2 L CO. Inset: Intensity of Pd 3d contributions versus CO exposure as obtained from fitting, 0.2 L is marked with a vertical line. The correlation of C 1s and Pd 3d species is shown schematically on the left.

The graphene signals are displayed in dark and light gray and the two CO-induced peaks, CO[a] and CO[b], are displayed in red and purple, respectively. The results of the fitting procedure for the two CO-induced signals are shown in the inset of Figure 4.5a. With beginning CO exposure the coverage of CO[a] increases until 0.5 L. At this exposure the coverage of CO[b] starts to increase while CO[a]

decreases by 18 %. In comparison with data of CO adsorbed on Pd single crystal surfaces, CO^a is assigned to CO adsorbed in highly coordinated adsorption sites like threefold hollow and step sites and CO^b is assigned to CO molecules adsorbed in lower coordinated adsorption sites like on-top and bridge sites.[36-37, 96] Due to the complex mixture of adsorption sites on the particles and the overlap of the asymmetric tail of the graphene signals with the CO signals, it is not possible to obtain more detailed information about the adsorption sites from the C 1s data.

For a more comprehensive analysis, the adsorption of CO on Pd nanoclusters was also followed in the Pd 3d region. Upon CO exposure the intensity of the Pd 3d bulk peak and the surface related peaks decrease and an additional CO-induced signal evolves. It is known from literature that the Pd 3d signal is very sensitive to adsorbates. With increasing CO exposure, the CO-induced signal continuously shifts to lower binding energies. The saturated Pd 3d spectrum exhibits two clearly separated signals: the bulk signal at 335.1 eV and a broad CO-induced signal at 335.9 eV. XP studies of CO on Pd(100) and Pd(111) revealed, that the binding energy shift of the Pd 3d signal is proportional to the number of bonds formed with CO.[36-37] In this study, three Pd 3d peaks with different relative binding energy shifts with respect to the bulk signal were employed to account for Pd atoms interacting with different numbers of CO molecules. An example fit of a Pd $3d_{5/2}$ spectrum of 0.7 ML Pd nanoclusters after exposure to 0.2 L CO is shown in Figure 4.5b. It contains the bulk contribution at 335.1 eV in black and the three CO-induced signals, $Pd–CO^\alpha$, $Pd–CO^\beta$, and $Pd–CO^\gamma$ in blue, orange and green, respectively. The binding energy shifts of the CO-induced signals with respect to the bulk signal are 0.36, 0.66 and 1.04 eV, respectively. The 0.36 eV shift of $Pd–CO^\alpha$ (blue) corresponds to interaction with one third of a CO molecule. The $Pd–CO^\alpha$ peak is therefore assigned to Pd atoms interacting with one CO molecule in a threefold hollow adsorption site. The binding energy shift of $Pd–CO^\beta$ (0.66 eV, orange) lies in between that of Pd atoms interacting with either one CO molecule in a bridge site – 0.51 eV on Pd(111) and 0.55 eV on Pd(100) – or with two CO molecules in threefold hollow sites – 0.70 eV on Pd(111). The $Pd–CO^\beta$ signal is therefore assigned to a mixture of such Pd atoms. Finally, the 1.04 eV shift of $Pd–CO^\gamma$ (green) corresponds to Pd atoms interacting with one CO molecule, i.e. one CO molecule at an on-top site or two CO molecules at bridge positions. The fitting results for the three CO-induced Pd signals are shown in the inset of Figure 4.5b. With CO exposure all three CO-induced Pd signals increase. However, the slope of the increase is steepest for

Pd–CO$^\alpha$ (blue) and the least steep for Pd–CO$^\gamma$ (green). After 0.1 L, the intensity of Pd–CO$^\alpha$ reaches its maximum and vanishes until 0.6 L. The Pd–CO$^\beta$ peak (orange) reaches its maximum at 0.3 L, and at saturation Pd–CO$^\gamma$ is the highest populated species. With increasing CO coverage the CO molecules become more densely packed on the surface of the Pd nanoclusters. Thus an increasing amount of Pd atoms interacts with more than one CO molecule. It is important to note that the contributions of the C 1s and Pd 3d regions cannot be directly translated into one another in this model, since one type of CO molecule can be associated with multiple contributions in the Pd region. The correlation between the different C 1s and Pd 3d contributions is shown schematically in the left part of Figure 4.5. From the similarity of both Pd 3d and C 1s spectra with XP data on Pd(111) and Pd(100) it is concluded that the Pd nanoclusters consist of a mixture of low-index facets and steps. The comparison of different Pd nanocluster samples containing varying amounts of deposited Pd revealed similar features in C 1s, O 1s and Pd 3d spectra. This similarity in spectral shape confirms the earlier finding that for higher Pd amounts the cluster density increases rather than the cluster size.

The thermal stability of CO on graphene-supported Pd nanoclusters was investigated with TP-XPS experiments in the C 1s and Pd 3d core level. The results show that CO adsorption is reversible, as CO desorbs completely from the Pd nanoclusters upon heating to 500 K. Differentiation of the total CO amount determined from the C 1s spectra yields desorption maxima at 230 and 430 K, independent of the deposited Pd amount. These values are in agreement with TPD results of CO on stepped Pd single crystal surfaces,[97] confirming that the nanoparticles consist of a mixture of low-index facets and steps. Detailed analysis of the Pd 3d spectra reveals restructuring of the nanoparticles during the first annealing process, similar as for the clean Pd nanoclusters. However, repeated adsorption of CO and heating to 500 K proved that the particles are stable after the first adsorption-desorption cycle.

In conclusion the properties of graphene-supported Pd nanocluster arrays were further explored by CO adsorption and desorption experiments. A detailed analysis of the C 1s, Pd 3d and O 1s core level spectra of several different Pd nanocluster samples with varying Pd amount confirmed that for higher Pd amounts the cluster density increases rather than the cluster size. From the fitting of C 1s and Pd 3d spectra a detailed description of the CO adsorption sites was derived. TP-XPS experiments showed that CO adsorption is reversible upon

heating to 500 K. The similarity of the XP spectra and agreement with TPD results on stepped surfaces confirm that the Pd nanoclusters consist of a mixture of low-index facets and steps.

4.3 Reactivity of Pt nanocluster arrays

4.3.1 <u>CO adsorption</u> [P6]

The adsorption of CO on 0.7 ML Pt at 150 K was investigated with HR-XPS. Upon CO exposure, three additional signals at 286.1, 286.5 and 286.7 eV are observed in the C 1s region, besides the characteristic two graphene and the carbide signals at 285.2, 284.5 and 283.8 eV, respectively. In order to see the CO-induced signals more clearly, the C 1s spectra are fitted and the graphene and carbide signals are subtracted from the raw data. The saturated spectrum and its fit after subtraction of the graphene and carbide signals are displayed in Figure 4.6e. The assignment of the three CO signals is made by comparison with single crystal data from previous studies (see Figure 4.6a-d).[35, 48-49] For a better understanding I will first briefly discuss the adsorption of CO on single crystals. On the flat Pt(111) surface, CO adsorbs at two different adsorption sites: on-top (286.8 eV) and bridge (286.0 eV). The saturated spectrum of CO on Pt(111) at 200 K is shown in Figure 4.6a.[35] At saturation, on-top and bridge sites are equally occupied. However, at lower coverage the occupation of on-top sites is clearly preferred. The occupation of bridge sites begins only after 65 % of the saturation coverage of CO^{on-top} is reached. The saturated and an unsaturated spectrum of CO on the stepped Pt(322) surface at 150 K are shown in Figure 4.6b and c, respectively.[49] In addition to the signals of CO adsorbed at on-top and bridge sites on the (111) terraces, two signals related to CO adsorption on the (100) steps are observed at 286.4 and 285.8 eV. They stem from adsorption at step on-top and step bridge sites, respectively. During CO adsorption, the step sites are occupied preferentially. In comparison to the flat Pt(111) surface, the preferential occupation of on-top sites over bridge sites is less pronounced on Pt(322). Due to the electronic influence of the steps, the adsorption energy difference of the two sites on the (111) terraces is smaller than on the flat single crystal. The saturated spectrum of CO on the stepped Pt(355) surface is displayed in Figure 4.6d.[48] Interestingly, only one step signal, with a similar binding energy as the step on-top signal on Pt(322), is observed on Pt(355). In comparison, the step signal on Pt(355) is more intense than on Pt(322). Again, steps are occupied preferentially during CO

adsorption, while the preferential occupation of on-top over bridge sites is even less pronounced than on Pt(322).
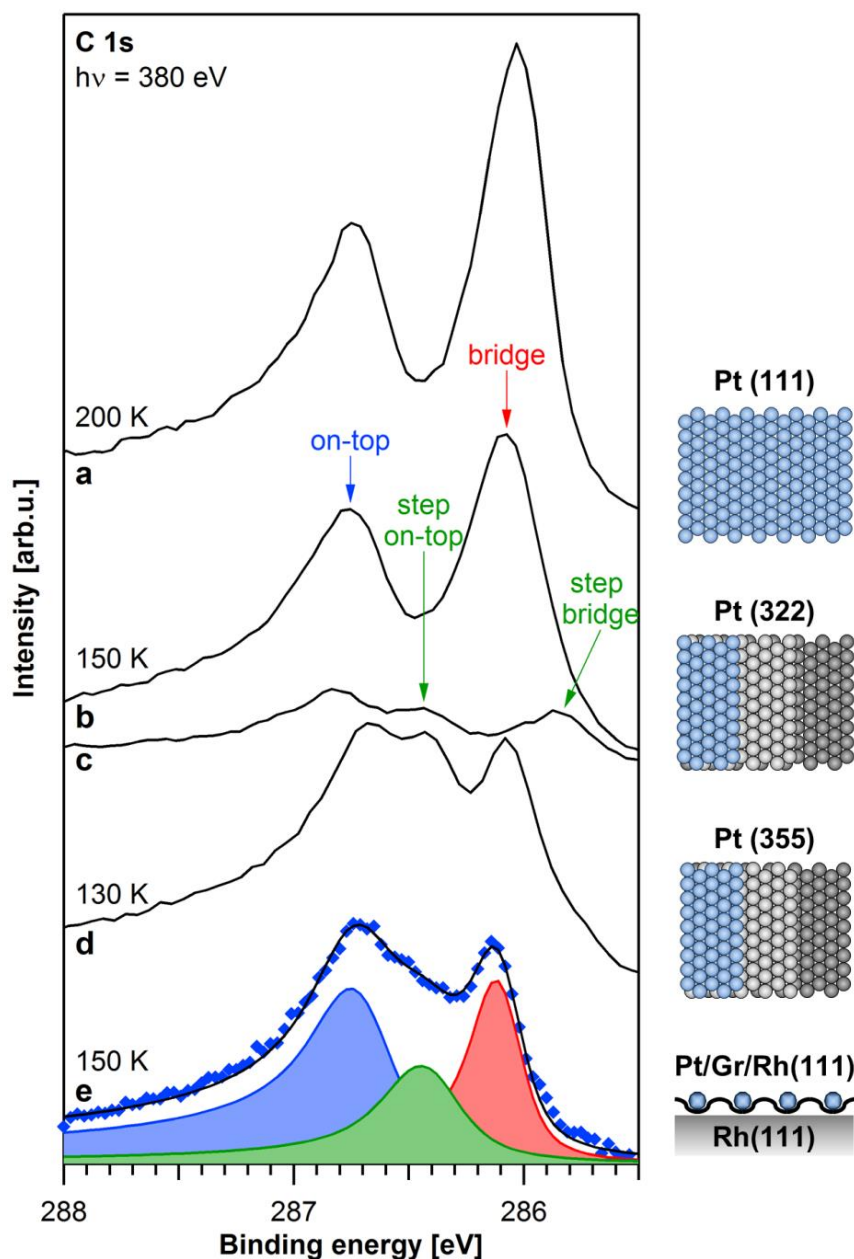

Figure 4.6: C 1s spectra of CO adsorbed on different Pt substrates. a) Saturated CO layer on Pt(111) at 200 K.[35] b) Saturated CO layer on Pt(322) at 150 K.[49] c) Unsaturated CO layer on Pt(322) at 150 K.[49] d) Saturated CO layer on Pt(355) at 130 K.[48-49] e) Saturated CO layer on 0.7 ML Pt nanoclusters on Gr/Rh(111) at 150 K; data points are shown as blue diamonds and the fit as a black line.

The saturated spectrum of CO adsorbed on graphene-supported Pt nanoclusters in Figure 4.6e shows the highest similarity with spectrum (d) on Pt(355). Therefore, the CO-induced signals are assigned accordingly. The CO signals were fitted with the same fitting parameters as for CO adsorbed on the

single crystal surfaces.[98] During adsorption of CO on graphene-supported Pt nanoclusters, a clear preference for the adsorption at step sites is observed. In contrast, the occupation of bridge sites starts only slightly after the occupation of on-top sites on the nanoclusters, indicating that the energy difference between on-top and bridge sites becomes very small on the cluster facets. The remarkable similarity with the XP spectra of the single crystal surfaces suggests the description of the Pt nanoclusters as a mixture of (111) facets and differently oriented steps, similar to the Pd nanoclusters. However, since the highest similarity is observed with the Pt(355) surface, probably mostly (111) steps are occupied. After the adsorption experiment, the thermal stability of CO on Pt nanoclusters was investigated by TP-XPS with a linear heating rate of 0.5 K/s. Upon heating, the on-top and bridge coverages decrease slowly until about 300 K, while the step coverage increases by 46 % in this temperature range. A similar increase of the step coverage was observed on the stepped Pt(322) surface.[49] This analogy verifies the presence of (100) steps as well as (111) steps. Until 450 K, CO adsorbed at on-top and bridge sites on the cluster facets desorbs completely. Finally, until 540 K also CO adsorbed at step sites desorbs completely. The significantly higher desorption temperature indicates that the step site is the most stable adsorption site. Both desorption temperatures are in excellent agreement with previous results on Pt(355).[48-49]

In conclusion, the comparison to Pt single crystal data leads to a clear assignment of the three CO-induced signals to CO adsorbed at on-top and bridge sites on the cluster facets and CO adsorbed at the cluster steps. As already established for the Pd nanoclusters, the graphene-supported Pt nanoclusters are described well by a mixture of (111) facets and both (111) and (100) steps. However, upon adsorption mostly (111) steps are occupied by CO. By comparison of the on-top over bridge site preference on the facets of the nanoclusters and the terraces on stepped and flat Pt single crystal surfaces it was found that the energy difference between the two adsorption sites becomes very small on the Pt nanoclusters.

4.3.2   Isothermal oxidation of CO [P6]

The isothermal oxidation of CO on 0.7 ML Pt on Gr/Rh(111) was investigated by HR-XPS in the O 1s core level at several different temperatures. Before the oxidation experiments, oxygen is preadsorbed at 200 K to ensure dissociation into atomic oxygen, yielding one asymmetric oxygen signal at 529.8 eV. CO is dosed

onto the sample with the molecular beam to provide a constant CO pressure of $2.6 \cdot 10^{-7}$ or $2.1 \cdot 10^{-6}$ mbar on the sample, while XP spectra are recorded. Upon CO exposure, two additional CO-induced signals evolve at 531.2 and 532.7 eV, which quickly saturate. Due to the overlap of the signals of CO adsorbed at step and at on-top sites in the O 1s core level, only one broad peak at 532.7 eV is observed. Simultaneously, the atomic oxygen signal decays due to reaction to CO_2 and rapid desorption thereof. As the focus of the kinetic analysis is on the decay of the oxygen signal, the deconvolution of the CO on-top and step signals does not present a problem.
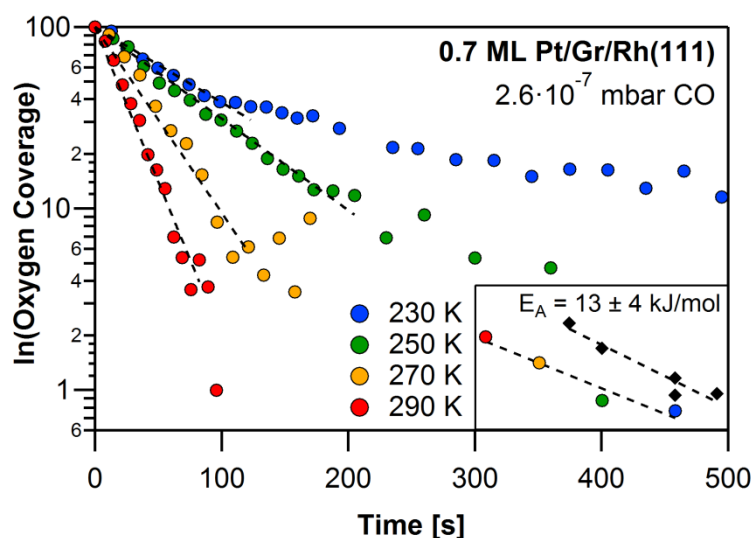

Figure 4.7: Logarithmic plot of normalized oxygen coverages from a series of isothermal oxidation experiments on 0.7 ML Pt/Gr/Rh(111) at $2.6 \cdot 10^{-7}$ mbar CO pressure and at different temperatures. Exponential fits are displayed as dashed black lines. The reaction rates obtained from the fits are displayed in an Arrhenius plot (ln[k] versus 1/T) in the inset (colored circles). The inset shows an additional data set obtained at a CO pressure of $2.1 \cdot 10^{-6}$ mbar (black diamonds). The average activation energy determined from the Arrhenius plot is 13 ± 4 kJ/mol.

The oxygen coverages of the complete temperature series at $2.6 \cdot 10^{-7}$ mbar CO are displayed in a logarithmic plot in Figure 4.7. The data between 250 and 290 K (green, orange and red) is described very well by exponential functions (dashed black lines in the logarithmic plot), indicating pseudo-first-order kinetics.[93] As the Pt surface is saturated quickly with CO, the local CO coverage is constant thereafter. Therefore, the reaction rate only depends on the oxygen coverage leading to the observed exponential decay. For the data recorded at 230 K (blue), the reaction proceeds more slowly after the first 100 seconds. This behavior is attributed to the lowered mobility of the adsorbates at this temperature.[99-100] After

neighboring reactants are consumed, the reaction proceeds more slowly, as the optimum reaction geometry is not reached fast enough. On account of this behavior only the first 100 s of the reaction at 230 K are described by an exponential fit (dashed black line). The reaction rates obtained from the dashed black fits are displayed in an Arrhenius plot in the inset of Figure 4.7. From this plot, an activation energy of 13.3 ± 4.0 kJ/mol is determined. The activation energy of 11.4 kJ/mol from the measurement series at 2.1 · 10^{-6} mbar CO pressure (black diamonds) falls well within the margin of error. In contrast, on the Pt(111) surface a 0.63 order rate law was found.[42] By STM and XPS measurements, it was established that the reaction mainly takes place at the edges of two-dimensional oxygen islands.[42, 101] The assumption of compact islands and reaction only at the edges leads to a reaction order of 0.5. Therefore, the reaction order on the Pt(111) surface is closer to 0.5 than to 1. Additionally, a faster reaction channel related to unordered oxygen was observed in the beginning of the reaction on Pt(111).[42] On the small facets of the Pt nanoclusters, the formation of oxygen islands does not play a role. Therefore, the simpler model of a pseudo-first-order rate law describes the reaction on the Pt nanoclusters sufficiently well. The fast reaction channel due to unordered oxygen on Pt(111) is likely related to the faster pseudo-first-order kinetics observed on the Pt nanoclusters. The activation energy of the same reaction on Pt(111) was determined to 51 ± 4 kJ/mol and 47 ± 4 kJ/mol, by XPS and STM, respectively.[42, 101] The much smaller activation energy on the Pt nanoclusters is attributed to the higher reactivity of the additional step and kink sites.

In conclusion, isothermal measurements with a supersonic molecular beam revealed pseudo-first-order kinetics of the CO oxidation on graphene supported Pt nanoclusters. The comparison to results on the Pt(111) surface suggests that the fast reaction on the clusters is related to unordered oxygen. An activation energy of 13 kJ/mol was determined, which is much smaller than on the Pt(111) single crystal surface, proving the high reactivity of Pt nanoclusters due to reactive step and kink sites.

4.3.3   SO$_2$ adsorption and reaction [P7]

The adsorption of SO$_2$ on 0.7 ML Pt on Gr/Rh(111) was investigated with HR-XPS. The results are again compared with data from previous studies on flat and stepped Pt single crystal surfaces. I will first summarize the results on Pt single crystal surfaces. On the flat Pt(111), surface SO$_2$ adsorbs in two different geo-

metries: either η^2 with the molecular plane perpendicular to the surface (standing, SO_2^{st}), or η^3 with the molecular plane parallel to the surface (lying, SO_2^{ly}).[41, 102] In the following, S 2p binding energies will be given in the form S $2p_{3/2}$ (S $2p_{1/2}$) eV. The spectrum of SO_2 adsorbed on Pt(111) at 130 K is displayed in Figure 4.8a.
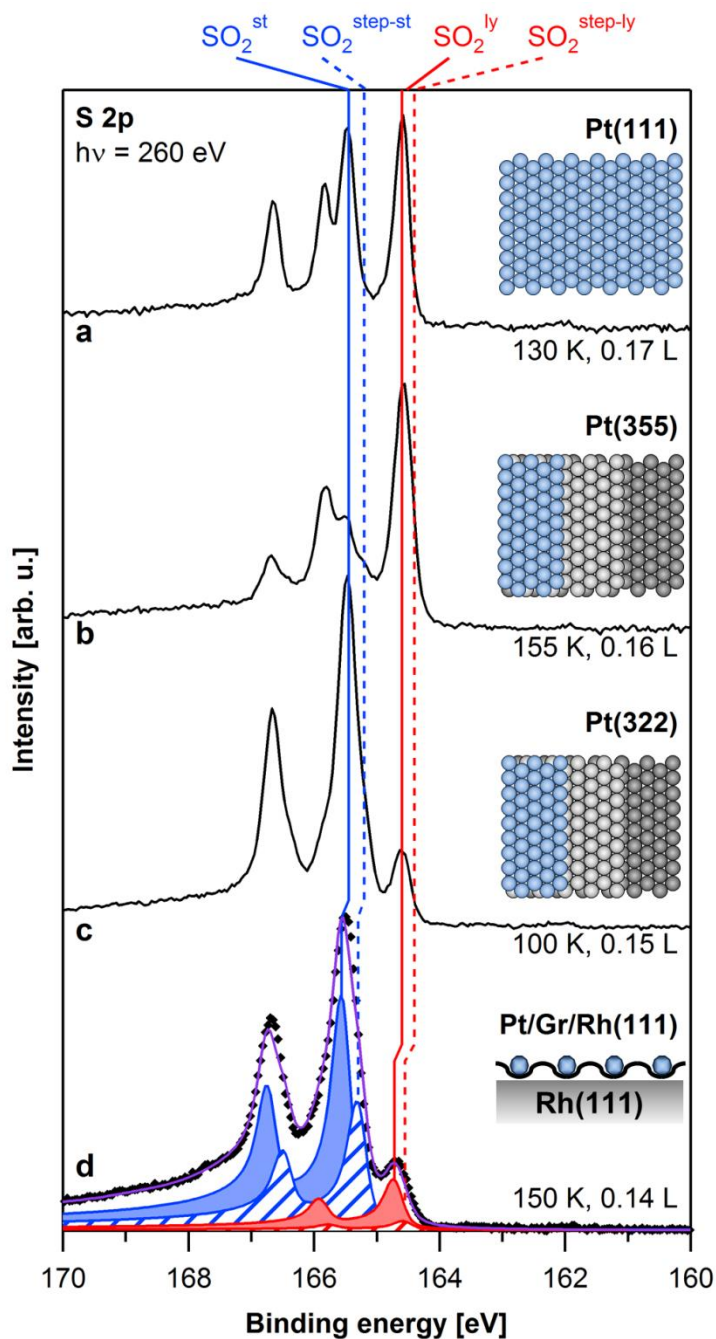

Figure 4.8: S 2p spectra of SO_2 adsorbed on different Pt substrates. The binding energies of S $2p_{3/2}$ signals are indicated with vertical lines. a) 0.17 L SO_2 on Pt(111) at 130 K,[41] b) 0.16 L SO_2 on Pt(355) at 155 K,[34] c) 0.15 L SO_2 on Pt(322) at 100 K,[34] and d) 0.14 L SO_2 on 0.7 ML Pt/Gr/Rh(111) at 150 K; The fit of the spectrum is shown in purple.

It consists of two doublets at 165.45 (166.67) and 164.60 (165.82) eV, assigned to SO_2^{st} and SO_2^{ly}, respectively. The binding energies of the S $2p_{3/2}$ signals are indicated by continuous blue and red lines, respectively. The ratio of $SO_2^{st} : SO_2^{ly}$ is 0.8 in this spectrum. Figure 4.8b shows a spectrum of 0.16 L SO_2 on Pt(355) at 155 K.[34] On this Pt surface, less SO_2 is bonded in standing geometry than in lying geometry on the (111) terraces of the crystal. This feature is attributed to the electronic influence of the steps. Additional intensity at 165.20 (166.42) and 164.40 (165.62) eV stems from SO_2 adsorbed at the steps of the crystal in standing ($SO_2^{step\text{-}st}$) and lying configuration ($SO_2^{step\text{-}ly}$). The S $2p_{3/2}$ binding energies of SO_2 adsorbed on the steps are indicated by a dashed blue and red line, respectively. In this spectrum, 13 % of the total SO_2 amount is adsorbed at steps, and the ratio of $SO_2^{st} : SO_2^{ly}$ is 0.4, considering SO_2 adsorbed at both terraces and steps. In Figure 4.8c a spectrum of 0.15 L SO_2 adsorbed on Pt(322) at 100 K is shown.[34] On this surface the situation is reversed: the signal of standing SO_2 is significantly higher than the one of lying SO_2. Apparently, the favored adsorption geometry of SO_2 on the terraces is governed by the step orientation. On Pt(322), SO_2 was found to adsorb only in standing configuration on the steps, comprising 19 % of the total SO_2 amount. The ratio of $SO_2^{st} : SO_2^{ly}$ is 5.6, again considering SO_2 adsorbed on the steps as well as the terraces. The spectrum of 0.14 L SO_2 on Pt nanoclusters at 150 K is shown in Figure 4.8d. The corresponding fit is shown in purple and the contributions of standing and lying SO_2 are displayed in blue and red, respectively. Contributions of SO_2 adsorbed at steps are shown hatched in the same respective color. The fitting parameters were adapted from those on Pt single crystals by adjusting the asymmetry and the Lorentzian width. In comparison to the single crystal surfaces, the SO_2 signals are shifted by 100-150 meV to higher binding energies. On the Pt nanoclusters, the favored adsorption geometry on the facets is standing, similar to the Pt(322) surface. The ratio of $SO_2^{st} : SO_2^{ly}$ on the clusters is 5.8. The high similarity with Pt(322) suggests the preferential occupation of (100) steps. However, the presence of $SO_2^{step\text{-}ly}$, which was not found on Pt(322) but on Pt(355), indicates that also (111) steps are occupied to some extent. Interestingly, this finding is contrary to the behavior found for CO on graphene-supported Pt nanoclusters, where (111) steps are occupied preferentially. This finding is attributed to the different adsorption behavior of the two adsorbates: while CO favors lower coordinated adsorption sites like on-top and bridge,[35, 103-104] SO_2 preferentially adsorbs at higher coordinated sites like threefold-hollow.[39, 105] These observations again confirm that the Pt nanoclusters consist of (111) facets and a mixture of

(100) and (111) steps. Depending on the adsorbate, either one or the other step geometry is occupied to a higher extent. Upon further adsorption of SO_2 on the Pt nanoclusters a multilayer signal at at 167.54 (168.73) eV evolves.

After SO_2 adsorption, the thermal reaction behavior was investigated with TP-XPS with a linear heating rate of 0.5 K/s. Upon heating to 200 K, the SO_2 multilayer desorbs. Additionally, a conversion of SO_2^{ly} to SO_2^{st} is observed, similar as on Pt(111) and to a lesser extent Pt(355).[34, 41] Subsequently, SO_2 diffuses onto the steps until 280 K and vanishes completely until 450 K. The most stable SO_2 species is $SO_2^{step-st}$, similar as on Pt(322). Starting around 200 K, an increasing amount of atomic sulfur is formed, which reaches a maximum value of 46 % of the initial SO_2 coverage. Between 270 and 475 K, also SO_3 is observed from the dis-proportionation of SO_2. In comparison to Pt single crystal surfaces, the tempera-tures, up to which SO_2 and SO_3 are observed, are significantly higher on the nanoclusters, indicating that both SO_2 and SO_3 are stabilized on the clusters. The amount of atomic sulfur on the nanoclusters is the highest observed for all inves-tigated Pt substrates, due to the high reactivity of the Pt nanoclusters.

In conclusion, a clear assignment of the S 2p signals observed during adsorption and reaction of SO_2 on graphene-supported Pt nanoclusters was made by comparison to single crystal surfaces. Two SO_2 adsorption geometries – standing and lying – were observed on both facets and steps of the Pt nano-clusters. In contrast to CO adsorption, (100) steps are occupied preferentially upon SO_2 adsorption. Upon annealing, diffusion of SO_2 to the steps as well as disproportionation to SO_3 and atomic sulfur was observed. The high amount of formed atomic sulfur confirms the high reactivity of the Pt nanoclusters. The obtained results further confirm that graphene-supported Pt nanoclusters consist of (111) facets and a mixture of (111) and (100) steps.

5 Summary

The interaction of sulfur and its oxides with the Pd(100) surface and the properties and reactivity of graphene-supported nanocluster arrays were investigated in detail by synchrotron-based HR-XPS. SO_2 adsorbs in two different geometries on the Pd(100) surface: standing and lying. Upon heating a stepwise reduction to SO and finally atomic sulfur is observed. On the oxygen-precovered Pd(100) surface, SO_3 is formed already upon adsorption at 116 K. In contrast to the clean surface, a stepwise oxidation to SO_3 and SO_4 is observed for the oxygen-precovered case. As SO_4 decomposes and desorbs at high temperatures, the surface is free of sulfur contaminations at 600 K. The oxidation of atomic sulfur proceeds stepwise to SO, SO_2, SO_3 and finally SO_4. The rate determining step thereby is the formation of SO with an activation energy of 85 ± 6 kJ/mol.

Graphene (Gr) on Rh(111) was produced by CVD. Subsequently, the quality of differently prepared graphene layers was checked by XPS, UPS and LEED. Exploration of a wide range of growth parameters showed that a sample temperature of 920 K and a carbon precursor pressure of $2 \cdot 10^{-8}$ mbar are ideal for the production of low defect density graphene. The oxidation of graphene on Rh(111) depends on the defect density and follows sigmoidal kinetics. Pd and Pt nanoclusters were deposited onto the Gr/Rh(111) template by electron beam evaporation. A combination of STM and HR-XPS revealed a template-assisted growth mode. The size and distribution of the nanoclusters is governed by the dimensions of the Moiré unit cell. For Pd clusters deposited at room temperature, the average diameter is 3 nm and the average height is three atomic layers. Stepwise annealing of Pd nanoclusters showed three different temperature regimes. Until 550 K, slight restructuring of the particles was observed, proving this temperature range well-suited for adsorption and reaction experiments. Up to 750 K agglomeration, and above this temperature intercalation of Pd between Rh and the graphene sheet occurs. The Pd nanoclusters were further probed by the adsorption of CO. The correlation of Pd 3d and C 1s signals allowed a detailed insight into the adsorption situation and suggested the description of the nanoclusters as a mixture of low-index facets and steps. Further evidence for a template-assisted growth of the clusters was provided by the survey of several cluster samples with varying Pd content. Temperature-programmed experiments showed that CO adsorption and desorption are reversible. Furthermore, the adsorption and temperature dependent behavior of CO and SO_2 on Pt nanocluster arrays was investigated in detail.

In both cases, comparison to results on flat and stepped Pt single crystal surfaces lead to a clear assignment of the observed surface species. Upon adsorption, CO preferentially occupies (111) steps, while SO_2 preferentially adsorbs at (100) steps due to the contrary preference for lowly and highly coordinated adsorption sites, respectively. The adsorption preference of CO at on-top over bridge sites is much lower on the nanocluster facets in comparison to single crystal surfaces, suggesting a significant electronic influence of the nanocluster steps. Annealing of CO covered Pt clusters leads to complete desorption of CO until 540 K. The observed desorption temperatures are in good agreement with those found on stepped single crystals. Upon heating of SO_2 covered Pt custers, SO_2 first diffuses onto the steps and disproportionates to SO_3 and S at higher temperatures. At 500 K, only atomic sulfur is left on the particles. The amount of sulfur left on the nanoclusters is significantly higher than on single crystal surfaces due to the enhanced reactivity of the clusters. For the isothermal oxidation of CO on Pt nanocluster arrays, pseudo-first-order kinetics associated with unordered oxygen were observed. An Arrhenius analysis yielded a much smaller activation energy than on Pt(111). In analogy to the Pd cluster arrays, the Pt clusters are described as a mixture of low-index facets and steps.

The altered stability of adsorption sites as well as the significantly higher reactivity prove that complex catalytic systems cannot simply be considered as a sum of their parts. Instead the interaction between all involved components has to be taken into account carefully. Under these conditions the advancement and analysis of model systems with increased complexity will lead to a comprehensive design and development of catalysts in the future.

6 Zusammenfassung

Die Adsorption und Reaktion von Schwefel und Schwefeloxiden auf der Pd(100) Oberfläche sowie die Eigenschaften und Reaktivität regelmäßig angeordneter Nanopartikel auf Graphen wurden mit hochaufgelöster Röntgenphotoelektronenspektroskopie (XPS) untersucht. Auf der Pd(100) Oberfläche adsorbiert SO_2 in zwei unterschiedlichen Geometrien: stehend, mit der Molekülebene senkrecht zur Oberfläche, und liegend, mit der Molekülebene parallel zur Oberfläche. Durch Erwärmung erfolgt eine schrittweise Reduktion zu SO und schließlich atomarem Schwefel. Ist die Pd(100) Oberfläche vor der Adsorption von SO_2 mit Sauerstoff bedeckt, bildet sich bereits bei der Adsorption SO_3. Im Gegensatz zur sauberen Oberfläche findet beim Heizen mit voradsorbiertem Sauerstoff eine schrittweise Oxidation zu SO_3 und SO_4 statt. Da sich SO_4 bei hohen Temperaturen zersetzt und anschließend desorbiert, ist die Oberfläche bei 600 K frei von Schwefelverunreinigungen. Die isotherme Oxidation von atomarem Schwefel läuft schrittweise über SO, SO_2 und SO_3 zu SO_4 ab. Der geschwindigkeitsbestimmende Schritt ist dabei die Bildung von SO mit einer Aktivierungsenergie von 85 ± 6 kJ/mol.

Graphen (Gr) wurde durch chemische Gasphasenabscheidung auf Rh(111) hergestellt. Die Qualität von Graphenschichten, die mit unterschiedlichen Parametern hergestellt wurden, wurde mit XPS, UPS und LEED kontrolliert. Die Variation verschiedener Wachstumsparameter zeigte, dass eine Wachstumstemperatur von 920 K und ein Präkursordruck von $2 \cdot 10^{-8}$ mbar ideal sind, um möglichst defektfreies Graphen herzustellen. Die Oxidation von Graphen auf Rh(111) ist von der Defektdichte abhängig und weist einen sigmoidalen Zeitverlauf auf. Pd und Pt Nanopartikel wurden durch Elektronenstoßverdampfung auf das Gr/Rh(111)-Substrat aufgedampft. Rastertunnelmikroskopie und XPS Ergebnisse belegen, dass die Moiréstruktur von Gr/Rh(111) als Templat für die Nanopartikel fungiert. Die Größe und Verteilung der Partikel ist durch die Dimensionen der Moiréeinheitszelle bestimmt. Für Pd Nanopartikel, die bei Raumtemperatur aufgedampft wurden, beträgt der gemittelte Durchmesser 3 nm und die durchschnittliche Höhe drei Atomlagen. Beim schrittweisen Heizen von Pd Nanopartikeln konnten drei Temperaturbereiche unterschieden werden. Bis 550 K findet nur geringfügige Umstrukturierung statt. Daher ist dieser Temperaturbereich für die Durchführung von Adsorptions- und Reaktionsexperimenten gut geeignet. Bis 750 K agglomerieren die Partikel und bei höheren Temperaturen interkaliert Pd zwischen dem Rh-Substrat und der Graphenschicht. Weiterhin wurden die Pd

Nanopartikel durch CO Adsorptionsexperimente charakterisiert. Die Korrelation von Pd 3d und C 1s Signalen ermöglichte eine detaillierte Beschreibung der Adsorption und zeigte, dass die Nanopartikel aus hochsymmetrischen Facetten und Stufen aufgebaut sind. Die Untersuchung mehrerer Proben mit unterschiedlich hohem Metallgehalt betätigte erneut, dass Gr/Rh(111) als Templat für die Nanopartikel fungiert. Die Reversibilität der CO Adsorption wurde mit Hilfe von temperaturprogrammierten Experimenten bewiesen. Weiterhin wurde das Adsorptionsverhalten von CO und SO_2 auf Pt Nanopartikeln analysiert. In beiden Fällen führt der Vergleich zu flachen und gestuften Pt Einkristalloberflächen zu einer klaren Zuordnung der beobachteten Oberflächenspezies. Während für CO die Besetzung von (111) Stufen bevorzugt ist, adsorbiert SO_2 bevorzugt an (100) Stufen, da für die Moleküle jeweils unterschiedlich stark koordinierte Adsorptionsplätze energetisch günstig sind. Auf Einkristalloberflächen sind „on-top" Adsorptionsplätze für CO gegenüber Brückenplätzen energetisch bevorzugt. Diese Energiedifferenz ist auf den Facetten der Nanopartikel auf Grund des elektronischen Einflusses der Stufen deutlich reduziert. Beim Erwärmen bis 540 K desorbiert CO vollständig von den Pt Partikeln. Die ermittelten Desorptionstemperaturen stimmen gut mit den Werten für gestufte Pt Einkristalloberflächen überein. Beim Erwärmen SO_2 bedeckter Pt Partikel, diffundiert SO_2 zuerst auf die Stufenplätze und disproportioniert bei höheren Temperaturen zu SO_3 und S, bis bei 500 K nur noch atomarer Schwefel übrig ist. Da die Partikel eine höhere Reaktivität als vergleichbare Einkristalloberflächen aufweisen, wird auf den Nanopartikeln deutlich mehr Schwefel gebildet. Die isotherme Oxidation von CO auf Pt Nanopartikeln verläuft nach einer Kinetik pseudo-erster Odnung, die durch die Anwesenheit von ungeordnetem Sauerstoff begründet ist. Durch die Anwendung der Arrhenius-Gleichung wurde auf den Nanopartikeln eine wesentlich kleinere Aktivierungsenergie als auf der Pt(111) Oberfläche bestimmt. Wie auch die Pd Partikel, bestehen die Pt Nanopartikel aus hochsymmetrischen Facetten und Stufen.

Die veränderte Stabilität einzelner Adsorptionsplätze und die deutlich höhere Reaktivität der Nanopartikel im Vergleich zu Einkristalloberflächen beweisen, dass die Nanopartikel mehr als nur die Anordnung verschiedener Facetten und Stufen sind. Die Beschreibung komplexer katalytischer Systeme als Summe ihrer Teile ist somit nicht ausreichend. Stattdessen müssen die Wechselwirkungen aller beteiligten Komponenten untereinander berücksichtigt werden. Auf diese Weise wird die Weiterentwicklung und Untersuchung von Modellsystemen die Entwicklung maßgeschneiderter Katalysatoren ermöglichen.

Literature

1.   H.-U. Blaser, A. Indolese, A. Schnyder, H. Steiner, M. Studer *J. Mol. Catal. A-Chem.* **2001**, *173,* 3.

2.   C. Marcilly *J. Catal.* **2001**, *216,* 47.

3.   M. Bowker *Chem. Soc. Rev.* **2008**, *37,* 2204.

4.   J. Han, D. Y. Zemlyanov, F. H. Ribeiro *Catal. Today* **2006**, *117,* 506.

5.   S. Royer, D. Duprez *Chem. Cat. Chem.* **2011**, *3,* 24.

6.   K. W. Kolasinski, *Surface Science - Foundations of Catalysis and Nanoscience*, Wiley, Chichester, **2012**.

7.   J. M. Thomas, W. J. Thomas, *Principles and Practice of Heterogeneous Catalysis*, VCH, Weinheim, **1997**.

8.   G. A. Somorjai, *Introduction to Surface Chemistry and Catalysis*, Wiley, New York, **1994**.

9.   U. Heiz, A. Sanchez, S. Abbet, W. D. Schneider *J. Am. Chem. Soc.* **1999**, *121,* 3214.

10.   F. Maillard, E. R. Savinova, U. Stimming *J. Electroanal. Chem.* **2007**, *599,* 221.

11.   M. Frank, S. Andersson, J. Libuda, S. Stempel, A. Sandell, B. Brena, A. Giertz, P. A. Brühwiler, M. Bäumer, N. Mårtensson, H.-J. Freund *Chem. Phys. Lett.* **1997**, *279,* 92.

12.   S. Schauermann, N. Nilius, S. Shaikhutdinov, H.-J. Freund *Accounts Chem. Res.* **2012**, *46,* 1673.

13.   H.-J. Freund *Surf. Sci.* **2002**, *500,* 271.

14.   G. N. Vayssilov, Y. Lykhach, A. Migani, T. Staudt, G. P. Petrova, N. Tsud, T. Skála, A. Bruix, F. Illas, K. C. Prince, V. Matolín, K. M. Neyman, J. Libuda *Nat. Mater.* **2011**, *10,* 310.

15.   D. W. Goodman *Appl. Surf. Sci.* **1984**, *19,* 1.

16.   P. Albers, J. Pietsch, S. F. Parker *J. Mol. Catal. A - Chem.* **2001**, *173,* 275.

17.   J. Oudar *Catal. Rev.* **1980**, *22,* 171.

18.   S. Ordóñez, P. Hurtado, F. V. Díez *Catal. Lett.* **2005**, *100,* 27.

19.   D. L. Mowery, M. S. Graboski, T. R. Ohno, R. L. McCormick *Appl. Catal. B - Environ.* **1999**, *21,* 157.

20.   S. Colussi, F. Arosio, T. Montanari, G. Busca, G. Groppi, A. Trovarelli *Catal. Today* **2010**, *155,* 59.

21.   T.-C. Yu, H. Shaw *Appl. Catal. B - Environ.* **1998**, *18,* 105.

22.   A. Shamsi *Catal. Today* **2009**, *139,* 268.

23.   A. V. Slack, G. A. Holliden, *Sulfur Dioxide Removal from Waste Gases*, Noyes Data Corp. , Park Ridge, NJ, **1975**.

24.   V.-M. Kerminen, L. Pirjola, M. Boy, A. Eskola, K. Teinilä, L. Laakso, A. Asmi, J. Hienola, A. Lauri, V. Vainio, K. Lehtinen, M. Kulmala *Atmos. Res.* **2000**, *54,* 41.

25.   G. Ertl *Angew. Chem.-Int. Ed.* **2008**, *47,* 3524.

26.   S. Hüfner, *Photoelectron Spectroscopy: Principles and Applications*, Springer, Berlin, **2003**.

27.   M. Henzler, W. Göpel, *Oberflächenphysik des Festkörpers*, Teubner, Stuttgart, **1994**.

28. D. P. Woodruff, T. P. Delchar, *Modern Techniques of Surface sSience*, Cambridge University Press, Cambridge, **1999**.

29. W. Berndt, R. Hora, M. Scheffler *Surf. Sci.* **1982**, *117,* 188.

30. G. Brodén, G. Pirug, H. P. Bonzel *Surf. Sci.* **1978**, *72,* 45.

31. I. Zasada, M. A. Van Hove *Surf. Rev. Lett.* **2000**, *07,* 15.

32. P. A. Thiel, E. D. Williams, J. T. Yates Jr, W. H. Weinberg *Surf. Sci.* **1979**, *84,* 54.

33. N. Luckas, K. Gotterbarm, R. Streber, M. P. A. Lorenz, O. Höfert, F. Viñes, C. Papp, A. Görling, H.-P. Steinrück *Phys. Chem. Chem. Phys.* **2011**, *13,* 16227.

34. R. Streber, C. Papp, M. P. A. Lorenz, O. Höfert, W. Zhao, S. Wickert, E. Darlatt, A. Bayer, R. Denecke, H.-P. Steinrück *J. Phys. Chem. C* **2010**, *114,* 19734.

35. M. Kinne, T. Fuhrmann, C. M. Whelan, J. F. Zhu, J. Pantförder, M. Probst, G. Held, R. Denecke, H.-P. Steinrück *J. Chem. Phys.* **2002**, *117,* 10852.

36. J. N. Andersen, M. Qvarford, R. Nyholm, S. L. Sorensen, C. Wigren *Phys. Rev. Lett.* **1991**, *67,* 2822.

37. S. Surnev, M. Sock, M. G. Ramsey, F. P. Netzer, M. Wiklund, M. Borg, J. N. Andersen *Surf. Sci.* **2000**, *470,* 171.

38. J. S. McEwen, S. H. Payne, H. J. Kreuzer, M. Kinne, R. Denecke, H.-P. Steinrück *Surf. Sci.* **2003**, *545,* 47.

39. M. Happel, N. Luckas, F. Viñes, M. Sobota, M. Laurin, A. Görling, J. Libuda *J. Phys. Chem. C* **2011**, *115,* 479.

40. R. Streber, C. Papp, M. P. A. Lorenz, A. Bayer, R. Denecke, H.-P. Steinrück *Angew. Chem. Int. Edit.* **2009**, *48,*

41. R. Streber, C. Papp, M. P. A. Lorenz, O. Höfert, E. Darlatt, A. Bayer, R. Denecke, H.-P. Steinrück *Chem. Phys. Lett.* **2010**, *494,* 188.

42. M. Kinne, T. Fuhrmann, J. F. Zhu, C. M. Whelan, R. Denecke, H.-P. Steinrück *J. Chem. Phys.* **2004**, *120,* 7113.

43. K. Gotterbarm, N. Luckas, O. Höfert, M. P. A. Lorenz, R. Streber, C. Papp, F. Viñes, H.-P. Steinrück, A. Görling *J. Chem. Phys.* **2012**, *136,* 094702.

44. S. Vajda, M. J. Pellin, J. P. Greeley, C. L. Marshall, L. A. Curtiss, G. A. Ballentine, J. W. Elam, S. Catillon-Mucherie, P. C. Redfern, F. Mehmood, P. Zapol *Nat. Mater.* **2009**, *8,* 213.

45. D. W. Goodman *Chem. Rev.* **1995**, *95,* 523.

46. H.-J. Freund, H. Kuhlenbeck, J. Libuda, G. Rupprechter, M. Bäumer, H. Hamann *Top. Catal.* **2001**, *15,* 201.

47. U. Diebold, N. Ruzycki, G. S. Herman, A. Selloni *Catal. Today* **2003**, *85,* 93.

48. B. Tränkenschuh, N. Fritsche, T. Fuhrmann, C. Papp, J. F. Zhu, R. Denecke, H.-P. Steinrück *J. Chem. Phys.* **2006**, *124,* 074712.

49. B. Tränkenschuh, C. Papp, T. Fuhrmann, R. Denecke, H.-P. Steinrück *Surf. Sci.* **2007**, *601,* 1108.

50. Ž. Šljivančanin, B. Hammer *Surf. Sci.* **2002**, *515,* 235.

51. M. Mavrikakis, M. Bäumer, H.-J. Freund, J. K. Nørskov *Catal. Lett.* **2002**, *81,* 153.

52. Y. O. Park, W. F. Banholzer, R. I. Masel *Appl. Surf. Sci.* **1984**, *19,* 145.

53. Y. O. Park, R. I. Masel, K. Stolt *Surf. Sci. Lett.* **1983**, *131,* L385.

54. J. Wintterlin, M.-L. Bocquet *Surf. Sci.* **2009**, *603,* 1841.

55. E. Voloshina, Y. Dedkov *Phys. Chem. Chem. Phys.* **2012**, *14,* 13502.

56. W. Zhao, S. M. Kozlov, O. Höfert, K. Gotterbarm, M. P. A. Lorenz, F. Vines, C. Papp, A. Görling, H.-P. Steinrück *J. Phys. Chem. Lett.* **2011**, *2,* 759.

57. R. J. Koch, M. Weser, W. Zhao, F. Viñes, K. Gotterbarm, S. M. Kozlov, O. Höfert, M. Ostler, C. Papp, J. Gebhardt, H.-P. Steinrück, A. Görling, T. Seyller *Phys. Rev. B* **2012**, *86,* 075401.

58. J. Gebhardt, R. J. Koch, W. Zhao, O. Höfert, K. Gotterbarm, S. Mammadov, C. Papp, A. Görling, H.-P. Steinrück, T. Seyller *Phys. Rev. B* **2013**, *87,* 155437.

59. A. B. Preobrajenski, M. L. Ng, A. S. Vinogradov, N. Martensson *Phys. Rev. B* **2008**, *78,* 073401.

60. M. Gao, Y. Pan, L. Huang, H. Hu, L. Z. Zhang, H. M. Guo, S. X. Du, H.-J. Gao *Appl. Phys. Lett.* **2011**, *98,* 033101.

61. J. Coraux, A. T. N'Diaye, C. Busse, T. Michely *Nano Lett.* **2008**, *8,* 565.

62. J. Coraux, A. T. N'Diaye, M. Engler, C. Busse, D. Wall, N. Buckanie, F. Meyer zu Heringdorf, R. van Gastel, B. Poelsema, T. Michely *New J. Phys.* **2009**, *11,* 023006.

63. C. Busse, P. Lazić, R. Djemour, J. Coraux, T. Gerber, N. Atodiresei, V. Caciuc, R. Brako, A. T. N'Diaye, S. Blügel, J. Zegenhagen, T. Michely *Phys. Rev. Lett.* **2011**, *107,* 036101.

64. M. Iannuzzi, J. Hutter *Surf. Sci.* **2011**, *605,* 1360.

65. E. N. Voloshina, Y. S. Dedkov, S. Torbrügge, A. Thissen, M. Fonin *Appl. Phys. Lett.* **2012**, *100,* 241606.

66. S. Marchini, S. Günther, J. Wintterlin *Phys. Rev. B* **2007**, *76,* 075429.

67. D. Martoccia, P. R. Willmott, T. Brugger, M. Björck, S. Günther, C. M. Schlepütz, A. Cervellino, S. A. Pauli, B. D. Patterson, S. Marchini, J. Wintterlin, W. Moritz, T. Greber *Phys. Rev. Lett.* **2008**, *101,* 126102.

68. B. Wang, S. Günther, J. Wintterlin, M. L. Bocquet *New J. Phys.* **2010**, *12,* 043041.

69. A. T. N'Diaye, S. Bleikamp, P. J. Feibelman, T. Michely *Phys. Rev. Lett.* **2006**, *97,* 215501.

70. A. T. N'Diaye, T. Gerber, C. Busse, J. Myslivecek, J. Coraux, T. Michely *New J. Phys.* **2009**, *11,* 103045.

71. K. Donner, P. Jakob *J. Chem. Phys.* **2009**, *131,* 164701.

72. Y. Pan, M. Gao, L. Huang, F. Liu, H.-J. Gao *Appl. Phys. Lett.* **2009**, *95,* 093106.

73. M. Sicot, S. Bouvron, O. Zander, U. Rüdiger, Y. S. Dedkov, M. Fonin *Appl. Phys. Lett.* **2010**, *96,* 093115.

74. B. Wang, B. Yoon, M. König, Y. Fukamori, F. Esch, U. Heiz, U. Landman *Nano Lett.* **2012**, *12,* 5907.

75. Z. Zhou, F. Gao, D. W. Goodman *Surf. Sci.* **2010**, *604,* L31.

76. H. Hertz *Ann. Phys.* **1887**, *267,* 983.

77. A. Einstein *Ann. Phys.* **1905**, *322,* 132.

78. R. Denecke, M. Kinne, C. M. Whelan, H.-P. Steinrück *Surf. Rev. Lett.* **2002**, *9,* 797.

79. A. Baraldi, G. Comelli, S. Lizzit, D. Cocco, G. Paolucci, R. Rosei *Surf. Sci.* **1996**, *367,* L67.

80. C. Papp, H.-P. Steinrück *Surf. Sci. Rep.* **2013**, *68,* 446.

81. S. Doniach, M. Šunjić *J. Phys. C Solid State* **1970**, *3,* 285.

82. D. Kolthoff, D. Jürgens, C. Schwennicke, H. Pfnür *Surf. Sci.* **1996**, *365,* 374.

83. E. Loginova, N. C. Bartelt, P. J. Feibelman, K. F. McCarty *New J. Phys.* **2009**, *11,* 063046.

84. E. Loginova, N. C. Bartelt, P. J. Feibelman, K. F. McCarty *New J. Phys.* **2008**, *10,* 093026.

85. Q. Yuan, J. Gao, H. Shu, J. Zhao, X. Chen, F. Ding *J. Am. Chem. Soc.* **2011**, *134,* 2970.

86. B. Wang, X. Ma, M. Caffio, R. Schaub, W.-X. Li *Nano Lett.* **2011**, *11,* 424.

87. B. Wang, M. Caffio, C. Bromley, H. Früchtl, R. Schaub *ACS Nano* **2010**, *4,* 5773.

88. I. Pletikosić, M. Kralj, P. Pervan, R. Brako, J. Coraux, A. T. N'Diaye, C. Busse, T. Michely *Phys. Rev. Lett.* **2009**, *102,* 056808.

89. J. Knudsen, P. J. Feibelman, T. Gerber, E. Grånäs, K. Schulte, P. Stratmann, J. N. Andersen, T. Michely *Phys. Rev. B* **2012**, *85,* 035407.

90. M. Kralj, I. Pletikosić, M. Petrović, P. Pervan, M. Milun, A. T. N'Diaye, C. Busse, T. Michely, J. Fujii, I. Vobornik *Phys. Rev. B* **2011**, *84,* 075427.

91. P. Sutter, J. T. Sadowski, E. Sutter *Phys. Rev. B* **2009**, *80,* 245411.

92. M. Sicot, P. Leicht, A. Zusan, S. Bouvron, O. Zander, M. Weser, Y. S. Dedkov, K. Horn, M. Fonin *ACS Nano* **2012**, *6,* 151.

93. J. E. House, *Principles of chemical kinetics*, Elsevier, Amsterdam, **2007**.

94. M. J. Gladys, A. A. El Zein, A. Mikkelsen, J. N. Andersen, G. Held *Surf. Sci.* **2008**, *602,* 3540.

95. J.-H. Gao, N. Ishida, I. Scott, D. Fujita *Carbon* **2012**, *50,* 1674.

96. M. G. Ramsey, F. P. Leisenberger, F. P. Netzer, A. J. Roberts, R. Raval *Surf. Sci.* **1997**, *385,* 207.

97. R. D. Ramsier, K. W. Lee, J. T. Yates Jr *Surf. Sci.* **1995**, *322,* 243.

98. B. Tränkenschuh, *Dissertation*, Erlangen, **2006**.

99. J. Hoffmann, S. Schauermann, J. Hartmann, V. P. Zhdanov, B. Kasemo, J. Libuda, H.-J. Freund *Chem. Phys. Lett.* **2002**, *354,* 403.

100. B. Brandt, T. Schalow, M. Laurin, S. Schauermann, J. Libuda, H.-J. Freund *J. Phys. Chem. C* **2006**, *111,* 938.

101. S. Völkening, J. Wintterlin *J. Chem. Phys.* **2001**, *114,* 6382.

102. M. Polcik, L. Wilde, J. Haase, B. Brena, G. Comelli, G. Paolucci *Surf. Sci.* **1997**, *381,* L568.

103. E. Schweizer, B. N. J. Persson, M. Tüshaus, D. Hoge, A. M. Bradshaw *Surf. Sci.* **1989**, *213,* 49.

104. H. Froitzheim, H. Hopster, H. Ibach, S. Lehwald *Appl. Phys.* **1977**, *13,* 147.

105. X. Lin, K. C. Hass, W. F. Schneider, B. L. Trout *J. Phys. Chem. B* **2002**, *106,* 12575.

List of abbreviations and symbols

AFM	**A**tomic **F**orce **M**icroscopy	**NC**	**N**ano**C**luster
CVD	**C**hemical **V**apor **D**eposition	**NEXAFS**	**N**ear **E**dge **X**-ray **A**bsoption **F**ine **S**tructure
DFT	**D**ensity **F**unctional **T**heory	**Pd**	**P**alla**d**ium
E_A	**A**ctivation **E**nergy	**Pt**	**P**la**t**inum
E_B	**B**inding **E**nergy	**QCM**	**Q**uartz **C**rystal **M**icrobalance
EELS	**E**lectron **E**nergy **L**oss **S**pectroscopy	**QMS**	**Q**uadrupole **M**ass **S**pectrometer
E_{kin}	**K**inetic **E**nergy	**Rh**	**Rh**odium
eV	**E**lectron **V**olt	**STM**	**S**canning **T**unneling **M**icroscopy
fwhm	**F**ull **W**idth at **H**alf **M**aximum	**TDS**	**T**hermal **D**esorption **S**pectroscopy
Gr	**Gr**aphene	**TP-XPS**	**T**emperature **P**rogrammed **X**-ray **P**hotoelectron **S**pectroscopy
h	Planck Constant		
HR-XPS	**H**igh **R**esolution **X**-ray **P**hotoelectron **S**pectroscopy	**UHV**	**U**ltra **H**igh **V**acuum
IRAS	**I**nfrared **R**eflection **A**bsorption **S**pectroscopy	**UPS**	**U**ltraviolet **P**hotoelectron **S**pectroscopy
J	**J**oule	**UV**	**U**ltra**V**iolet
K	**K**elvin	**XPS**	**X**-ray **P**hotoelectron **S**pectroscopy
L	**L**angmuir ($1.33 \cdot 10^{-6}$ mbar $\cdot$ s)		
LEED	**L**ow **E**nergy **E**lectron **D**iffraction	Φ	Workfunction
ML	**M**ono**L**ayer	ν	frequency

Curriculum Vitae

KARIN BRIGITTE GOTTERBARM

Geboren am 01. Juli 1987 in München

Promotion

| seit 05/2011 | am Lehrstuhl für physikalische Chemie II der Friedrich-Alexander-Universität Erlangen-Nürnberg (FAU) |

Studium

03/2011	Abschluss Master of Science
09/2009 – 03/2011	Masterstudium Molecular Nano Science an der FAU
08/2009	Abschluss Bachelor of Science
09/2006 – 08/2009	Bachelorstudium Molecular Nano Science an der FAU

Schulische Ausbildung

06/2006	Erwerb der allgemeinen Hochschulreife
05/1999 – 06/2006	Emil-von-Behring-Gymnasium in Spardorf
09/1997 – 05/1999	Friedrich-Abel-Gymnasium in Vaihingen an der Enz
08/1993 – 07/1997	Grundschule in Vaihingen an der Enz

Danksagung

Appendix: [P1] – [P7]

[P1]   *Adsorption and Reaction of SO₂ on Clean and Oxygen Precovered Pd(100) – a Combined HR-XPS and DF Study*

Nicola Luckas, **Karin Gotterbarm**, Regine Streber, Michael P. A. Lorenz, Oliver Höfert, Francesc Viñes, Christian Papp, Andreas Görling, Hans-Peter Steinrück

Physical Chemistry Chemical Physics 13 (36) **2011** 16227–16235.

[P2]   *Kinetics of the Sulfur Oxidation on Palladium: A Combined In Situ X-Ray Photoelectron Spectroscopy and Density-Functional Study*

Karin Gotterbarm, Nicola Luckas, Oliver Höfert, Michael P. A. Lorenz, Regine Streber, Christian Papp, Francesc Viñes, Hans-Peter Steinrück, Andreas Görling

The Journal of Chemical Physics 136 (9) **2012** 094702.

[P3]   *Growth and Oxidation of Graphene on Rh(111)*

Karin Gotterbarm, Wei Zhao, Oliver Höfert, Christoph Gleichweit, Christian Papp, Hans-Peter Steinrück

Physical Chemistry Chemical Physics 15 (45) **2013** 19625–19631.

[P4]   *Graphene-Templated Growth of Pd Nanoclusters*

Karin Gotterbarm, Christian Steiner, Carina Bronnbauer, Udo Bauer, Hans-Peter Steinrück, Sabine Maier, Christian Papp

The Journal of Physical Chemistry C 118 (29) **2014** 15934–15939.

[P5]   *Graphene-Supported Pd Nanoclusters Probed by Carbon Monoxide Adsorption*

Karin Gotterbarm, Carina Bronnbauer, Udo Bauer, Christian Papp, Hans-Peter Steinrück

The Journal of Physical Chemistry C 118 (43) **2014** 25097–25103.

[P6]   *Reactivity of Graphene-Supported Pt Nanocluster Arrays*

Karin Gotterbarm, Florian Späth, Udo Bauer, Carina Bronnbauer, Hans-Peter Steinrück, Christian Papp

ACS Catalysis 5 (4) **2015** 2397–2403.

[P7]   *Adsorption and reaction of SO₂ on graphene-supported Pt nanoclusters*

Karin Gotterbarm, Florian Späth, Udo Bauer, Hans-Peter Steinrück, Christian Papp

Topics in Catalysis 58 (10–11) **2015** 573–579.